Local strain redistribution in a coarse-grained nickel-based superalloy subjected to shot-peening, fatigue or thermal exposure investigated using synchrotron X-ray Laue microdiffraction

G. Altinkurt[1,2], M. Fèvre[1,*], G. Geandier[2], M. Dehmas[3], O. Robach[4,5], and J.-S. Micha[4,5,6]

[1] Laboratoire d'Étude des Microstructures, UMR 104 CNRS-ONERA, 92322 Châtillon, France
[2] IJL, UMR 7189 CNRS-Université de Lorraine, Nancy, France
[3] CIRIMAT, UMR 5085 CNRS-UPS-INPT-ENSIACET, 31000 Toulouse, France
[4] Université Grenoble Alpes, 38000 Grenoble, France
[5] CEA-INAC-MEM, 17 rue des Martyrs, 38000 Grenoble, France
[6] CNRS, 17 rue des Martyrs, 38000 Grenoble, France

ABSTRACT

The Laue microdiffraction technique was used to investigate the strain field caused by the shot-peening operation and its redistribution after thermal hold or fatigue in a model nickel-based superalloy with an average grain size of 40 μm. Micrometer and millimeter size mappings showed that the plastic deformation introduced by shot-peening in the whole sample partially relaxes after a thermal exposure at 450°C and was fully redistributed by the fatigue of the material, except in the hardened layer close to the sample edge. Diffraction patterns permitted to measure separately the strains related to the average alloy ($\gamma + \gamma'$) and to the γ' phase. No difference was observed between the two deviatoric strain fields. Even if there were small stresses in the inner part of the samples, the sensitivity of the Laue microdiffraction method was large enough to quantitatively characterize the crystal misorientations and the deviatoric strain redistributions. Useful data were provided not only at the grain scale but also at the mesoscopic scale, thus bridging the gap between the $\sin^2\psi$ and Ortner's methods used to determine residual stresses, respectively, in fine and single-grain microstructures. The obtained results are also of first interest for a quantitative comparison with HR-EBSD measurements in the scanning electron microscope. Energy coupled measurements with an energy-dispersive point detector were also performed to determine the full elastic strain tensors associated with the γ and γ' phases. We demonstrated that, for Ni-based superalloys, the accuracy on strains and stresses was, respectively, of the order of 1×10^{-3} and 250 MPa for the diagonal components of tensors. The measurements suffered from the 150 eV

Address correspondence to E-mail: Mathieu.Fevre@onera.fr

https://doi.org/10.1007/s10853-018-2144-4

resolution of the detector which made it difficult to the separate the energies of the γ and γ' phases. Owing to large crystal misorientations, the microdiffraction technique was not able to determine elastic strains and hardening in the highly deformed layer, where a large amount of plastic strain and a number of defects were accumulated. Some improvements are proposed to overcome these difficulties.

Introduction

Knowledge of the fatigue behavior of aeronautical high-pressure turbine (HPT) disks is crucial to avoid bursts and uncontained engine failures. The low-cycle fatigue life of such components made of polycrystalline nickel-based superalloys is primarily influenced by the amplitude of applied loads and by the alloy microstructure (e.g., chemical composition, grain size, volume fraction of phases) [1]. The surface roughness and residual stresses inherent to the manufacturing process or imposed by the surface treatment also affect the component lifetime (e.g., shot- and laser-peening, deep rolling). Owing to the complex thermal and mechanical repeated cyclic loading conditions during the engine service, the initial stress field may relax, be redistributed or evolve, particularly at high temperature (see [2] and references therein). Nonlinear elasto-viscoplastic models coupled to creep and a fatigue damage model [3] enable the identification of fatigue critical zones and crack initiation time, depending on the thermal and mechanical history of the disk [4]. The improvement of such lifetime analysis is nowadays realized through the development of methods that take into account residual stresses and can predict their static and cyclic relaxation [5].

At a macroscopic scale, the relaxation or the redistribution of stresses induced by shot-peening was investigated in depth at different temperatures in the Inconel, Astroloy and Udimet superalloys after isothermal treatments or fatigue loadings [6–9]. The measurements were taken using the $\sin^2\psi$ method and electrochemical polishing for material removal. The authors have shown that in the surface layer affected by the shot-peening operation, some significant fraction of the initial residual stresses relaxes in the first hour of isothermal holding [9] or in the first cycle of a fatigue loading [8]. Stresses are usually obtained with millimeter-sized incoming beams from the diffraction of several thousand grains by the crystal lattice planes corresponding to fundamental reflections. Due to the large amount of plastic deformation and the small lattice mismatch between the two phases, the results are related to the average alloy (γ-matrix and γ'-precipitates) accordingly. Although measurements with high-resolution spectrometers at the laboratory or in large facilities have been taken to separate the γ and the γ' contributions for determining lattice misfits or microstrains in polycrystals [10–13], such an analysis has not been reported for residual stresses arising from shot-peening. Numerically, some models have been developed to predict stress relaxations in Astroloy and IN100 nickel-based superalloys under thermal and thermomechanical solicitations with rather good agreement with experimental data [6, 14].

At a lower scale, the characterization and modeling of crack nucleation and growth in powder metallurgy alloys are also deeply investigated to understand the physical mechanisms responsible for the damage of materials in relation to the microstructure (e.g., grain size distribution and crystal defects). However, the effects of shot-peening and related strain redistribution after isothermal treatment or fatigue are poorly documented [15–17]. Child et al. [15] demonstrated that the grain orientation spread (GOS) calculated from the orientation measurements by electron backscattered diffraction (EBSD) can be used to understand the work hardening induced by shot-peening. However, Foss et al. [16] have observed that the depth of work hardening determined with an EBSD analysis was half of the one measured using microhardness tests or X-ray diffraction peak widths. Dislocation structures due to shot-peening were observed by transmission electron microscopy after heat treatment [18] or fatigue loading [17] in order to investigate the effect of temperature, time and loading conditions on their annihilation. The main relevant point was that although the residual compressive stresses are largely relieved during the

first fatigue cycle, a high dislocation density is retained close to the sample surface, even after 3×10^6 cycles at 700°C, and the effectiveness of shot-peening persists. Numerically, Musinski and McDowell [19] have used the eigenstrain formalism to introduce residual stresses associated with shot-peening in a crystal plasticity model and have predicted stress relaxations in IN100 after a single loading/unloading sequence. Owing to the lack of experimental data at the grain scale, the comparison with the $\sin^2\psi$ measurements involved numerical averages over grains and the origin of discrepancies was not easy to localize. To improve these models, high-angular-resolution electron backscatter diffraction (HR-EBSD) in a laboratory or X-ray microdiffraction experiments in a synchrotron can measure residual elastic strains inside the grains and geometrically necessary dislocation (GND) densities [20]. At this scale, total strains can be determined using the recently developed FIB-DIC ring core method which combines FIB milling and digital image correlation (DIC) [21–23]. The method was applied to determine residual stresses arising from shot- peening operation at different locations in aluminum notched specimens [24] and in a nickel-based compressor blade [23].

The previous review shows that in polycrystalline superalloys, quantitative data about the strain field arising from the shot-peening operation and its redistribution under thermal and mechanical conditions are not available at the grain scale. The characterization of microstrains related to the γ matrix and the γ' phase after pre-stress treatments is also missing. Such information would (1) provide a better understanding of the relationship between the alloy microstructure and damage resistance and (2) facilitate the development more physically justified models (e.g., crystal plasticity- or dislocation dynamics-based models). Stress measurements at the millimeter scale are also needed by continuum mechanics models taking into account the specific geometry of the mechanical components and surface treatments. The aim of this study is to address these issues using X-ray microdiffraction measurements (μXRD) on samples that were subjected to shot-peening, isothermal holding and fatigue. Measurements are taken in a N18 alloy where the 10 μm initial average grain size is modified to 40 μm. Increasing the grain size (GS) is a way to improve the mechanical properties of HPT disks at high temperature (creep or crack propagation resistance). The determination of residual stresses in coarse-grained microstructures ($30\,\mu m < GS < 500\,\mu m$) using diffraction-based techniques is challenging because of the limitations of the most common measurement techniques ($\sin^2\psi$ [25] and Ortner's [26] methods). The $\sin^2\psi$ method can be employed in such microstructures if a sufficient number of grains diffract. This can be performed using high-energy X-rays or neutrons experiments or by oscillating the sample when beams with a smaller penetration depth into the material are used. Then, measured quantities correspond to averages in mm^3 or cm^3 gauge volumes. The Ortner's method employs a monochromatic beam and requires measuring about 20 Bragg angles arising from the same crystallite [27, 28]. The method is not adapted to grain sizes lower than 100 μm due to (1) the uncertainties caused by the movements of the goniometer and (2) the amount of time which would be required to investigate many grains of a polycrystal. The μXRD method uses a sub-micrometric beam size and a polychromatic beam. This enables to record, without any motion of the diffractometer and in a single shot, many diffraction spots which are necessary to determine elastic strains with a good accuracy. For coarse-grained microstructures, the grain size is thus no longer an issue. This work aims to improve the characterization and the understanding of stress relaxations in high-temperature alloys for aero engine applications and to assess the ability of the Laue microdiffraction technique to quantify residual stresses in coarse-grained microstructures.

The article is organized as follows. The samples and experimental detail are presented in "Materials and methods" section. The deviatoric strain fields obtained for the reference, the shot-peened, the heat treated and the fatigued mechanical states are analyzed in "Initial state", "Shot-peened state", "Strain redistribution after an isothermal holding" and "Strain redistribution after fatigue" sections. Full strain measurements are described in "Full strain tensor measurements" section. Finally, a discussion highlighting the redistribution of residual stresses and the crystal misorientations after the thermal and the mechanical loadings is provided in "Discussion" section.

Materials and methods

Material preparation and samples

Cylindrical specimens were removed using electro-discharge machining in a sector of high-pressure turbine disk made of the N18 nickel-based superalloy produced with a powder metallurgy route at Safran Aircraft Engines (see composition in Table 1). The heat treatment was identical to that reported in Ref. [29]. Optical microscopy observations revealed that the as-received microstructure was mainly characterized by a 10 µm average grain size and 3 populations of γ' precipitates ($L1_2$ simple cubic structure) embedded into the γ matrix (A1 face-centered cubic structure). To simplify the analysis of the diffracted intensities associated with the γ' phase, a coarse-grained microstructure with a single population of intragranular γ' precipitates was obtained after a supersolvus solution treatment of 4 h at 1205°C followed by an air quench and an aging treatment of 1 h at 900°C followed by an air quench. The average grain size determined by EBSD on a 6 mm × 6 mm area using a 3-µm step size was 40 µm with a distribution ranging from 5 to 200 µm. The average precipitate size was 200 nm with a distribution between 40 and 400 nm. The volume fraction of the γ' precipitates measured using a Rietveld analysis was 44%. Figure 1 represents an example of the γ grain and γ' precipitate structure of the N18 alloy obtained in a SEM by EBSD analysis and secondary electron imaging. It is worth mentioning that some abnormal grain growth may take place during the solution treatment of the samples. Therefore, some grains can exhibit sizes larger than 200 µm in the investigated microstructures.

Table 1 Chemical composition (in weight %) of the N18 nickel-based superalloy

Ni	Co	Cr	Mo	Al	Ti	Hf	Zr	B	C
Bal.	15.5	11.4	6.4	4.5	4.5	0.5	0.03	0.02	0.01

In the first instance, five cylindrical specimens were machined for fatigue testing. The gauge length was 14 mm, the gauge diameter was 6.2 mm, and the radius of the transition to the M11 screw threads was 20 mm. A specimen was used as reference sample, and the others were subjected to shot-peening, isothermal holding and/or fatigue conditions as summarized in Table 2. Ultrasonic shot-peening (USP) was realized on the circumference of the cylindrical specimens (gauge section and transitions to the screw thread) with 3-mm-diameter 100Cr6 steel shots for 18 min. These conditions were chosen to have a coverage close to 100% and to introduce strain fields with characteristic wavelengths larger than the grain size. Low-cycle fatigue (LCF) tests were performed at 450°C with a cyclic frequency of 1 Hz and an imposed axial total strain varying in the range of 0–1%. These parameters correspond to a regime where plasticity is mainly accumulated during the first loading cycle. A small amount of plastic

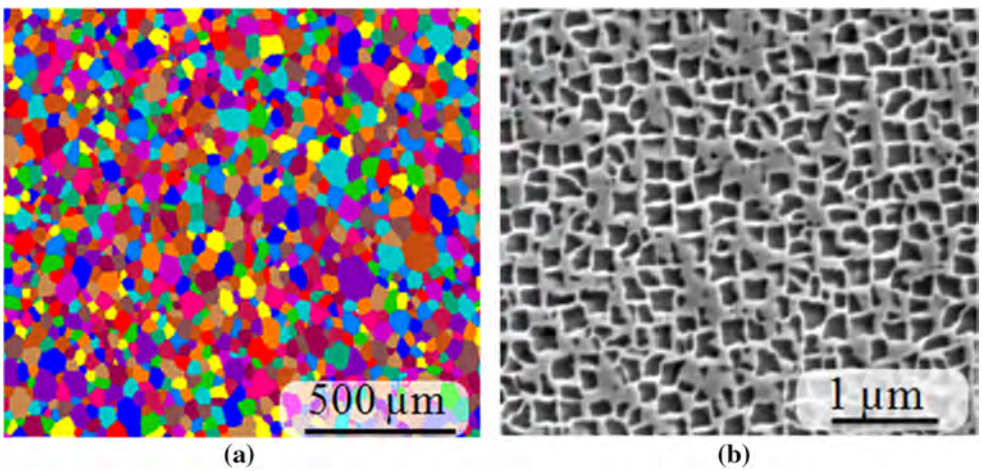

Figure 1 Observation of the coarse-grained microstructure in the N18 superalloy. **a** EBSD map revealing γ grains (random colors) with an average size of 40 µm. **b** Secondary electron image showing γ' precipitates (dark gray) with an average size of 200 nm embedded in the γ matrix (light gray).

Table 2 Summary of the different heat and mechanical treatments applied to the fatigue test specimen and the corresponding sample labels used in the text

Label	Mechanical and/or heat treatments
S1	None
S2	USP at room temperature
S3	USP + hold at 450°C during 1 h 40 min
S4	USP + LCF at 450°C during 1 h 40 min
S5	LCF at 450°C during 1 h 40 min

USP ultrasonic shot-peening; *LCF* low-cycle fatigue

deformation is further accumulated at each cycle (see detail in "Appendix 1"). As shown by John et al. [9] in the IN100 superalloy, the residual stresses caused by the shot-peening operation may be fully relaxed at the failure of the specimen. In the absence of such data for the N18 alloy, the LCF tests were interrupted after 300 cycles (i.e., 1 h 40 min). This value corresponds to approximately 25% of the fatigue lifetime of an unpeened specimen [4]. After the thermal and mechanical treatments, the test sections were cut to obtain cylinders with 10 mm height (see Fig. 2). Cross sections were then mechanically and chemically polished to remove the stresses induced by the machining operation. For this purpose, SiC grinding papers of Grades 1000–4000 were successively employed. Then, a polishing was realized with a 0.25 µm diamond paste. A 15-µm thick layer was finally removed electrochemically with a methanol solution containing 17% of sulfuric acid. The Laue microdiffraction technique was then used to map the strain fields and the crystalline misorientations on one of the two cross sections. µXRD measurements were taken on a reference sample which has been polished as described above and on a reference sample which has been polished with the grinding papers only. The comparison of the deviatoric elastic strain maps (2.5 mm × 1 mm) recorded with a 50-µm step size did not show any difference attributable to the sample surface preparation. However, full stress relaxations due to polishing may not be excluded especially at the grain boundaries. This effect was not investigated in the present work.

X-ray Laue microdiffraction

µXRD measurements were taken in the BM32 French CRG-IF beamline at the ESRF [30]. The incoming 5–22 keV polychromatic beam was focused with Kirkpatrick–Baez mirrors to have a $0.35 \times 0.6\,\mu m^2$ size on the sample surface, which was tilted by 40° with respect to the X-ray beam (Fig. 2). The absorption length of the beam into the material was in a 5−15 µm range, depending upon the photon energy and the angle of diffracted beams with respect to the sample surface. The diffraction patterns were collected with a 2048 × 2048 pixels MAR165 circular CCD detector located 70 mm above the sample. Owing to the grain and beam sizes, Laue patterns were composed of diffraction spots originating from one or a few grains. During each acquisition, the incoming beam, the sample and the detector were in fixed positions. The mapping of the sample surface was realized with a motorized *xyz* linear translation stage. To measure the energy of specific Laue spots, a fluorescence spectrum was collected using a silicon drift Ketek Vitus H7 detector mounted upon an *yz* linear translation stage on the sample side [31].

The experimental geometry calibrations and the diffraction pattern analyses were performed using the *LaueTools* software developed by the BM32 beamline staff of the ESRF [32]. Given a crystal structure, the (*hkl*) Miller indices of Laue spots arising from the same grain were obtained by matching the experimental pattern with simulated ones (Fig. 3b). The indexing process considers the spots with the highest intensity first. This means that indexed grains are not necessarily at the sample surface but can be deeper into the material (in the 5−15 µm range). The grain size distribution of Fig. 1 revealed that about 10% of grains were in the 5−15 µm interval. If several grains are indexed in the depth probed by the X-ray beam, the information about the depth of these grains is not known although the accuracy of the measured strains is approximately 2×10^{-4}. To know which grain is at the sample surface, the grain orientation obtained by the Laue technique can be compared to the one obtained using EBSD. Alternatively, the differential aperture X-ray microscopy (DAXM) [33, 34] can be coupled to the Laue measurements at the expense of much higher acquisition times. If there is only one grain probed by the X-rays, strains are integrated over the penetration depth. A depth resolution can be provided by the DAXM, or if a sufficiently large number of Laue spots are collected, by indexing the Laue spots which are associated to a constant penetration depth. This issue is out of the

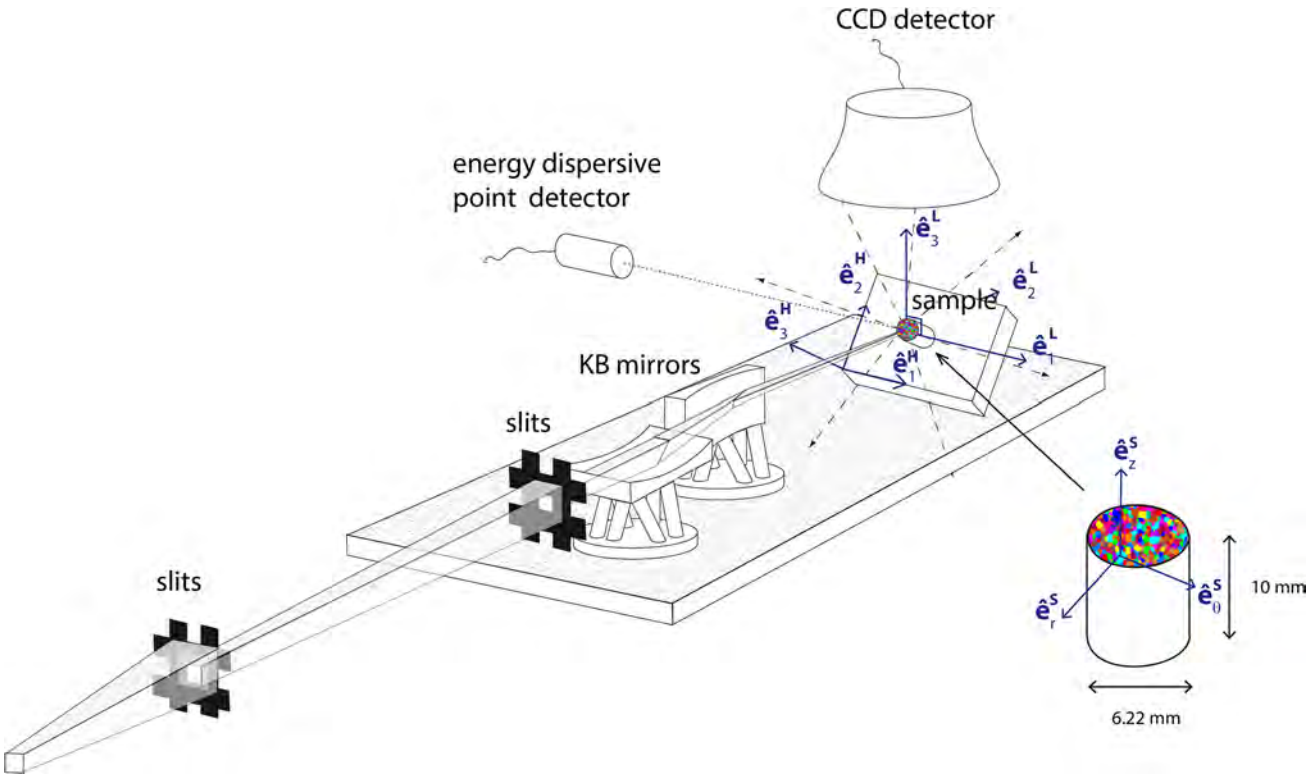

Figure 2 Schematic of the diffractometer setup with polychromatic incident X-ray beam, slits, Kirkpatrick–Baez focusing mirrors (KB) mounted on hexapods, polycrystalline sample, 2D CCD detector and energy-dispersive point detector. $(\hat{\mathbf{e}}_1^L, \hat{\mathbf{e}}_2^L, \hat{\mathbf{e}}_3^L)$, $(\hat{\mathbf{e}}_1^H, \hat{\mathbf{e}}_2^H, \hat{\mathbf{e}}_3^H)$ are the fixed Cartesian coordinate systems of the laboratory and the sample holder. $(\hat{\mathbf{e}}_r^S, \hat{\mathbf{e}}_\theta^S, \hat{\mathbf{e}}_z^S)$ is the cylindrical coordinate system related to the sample. The trajectories of the diffracted beams are symbolized by the multidirectional dashed arrows (see text for detail). Dotted lines are guidelines.

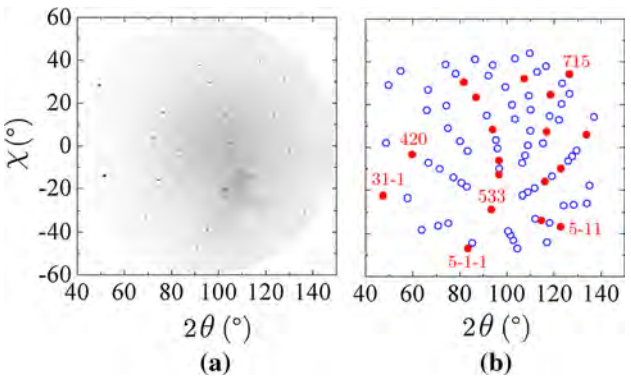

Figure 3 Laue patterns in the CDD detector coordinate system $(2\theta, \chi)$. **a** Raw data. **b** Simulated pattern with the fundamental (closed symbols) and superstructure (open symbols) reflections.

scope of the present study. Once the pattern indexed, scalar products of four non-collinear diffraction unit vectors corresponding to reflections of known Miller indices enable the expression of the reciprocal lattice vectors in the laboratory coordinate system [35]. The coordinates of the crystal lattice vectors were finally obtained by the Fourier transform. This led to the determination of the crystal orientation matrix and the unit cell parameters $(b/a, c/a, \alpha, \beta, \gamma)$. Owing to the fact that energy discrimination is not possible with the used CCD detector, the energy of Bragg spots is unknown and the a cell parameter is not determined. Assuming that the deformed unit cell has the same volume as the undeformed unit cell, the six independent components of the deviatoric strain tensor, denoted by ε_{ij}^d $(i, j = 1, 2, 3)$, can be calculated within the small transformation hypothesis in the crystal system of coordinates. Then, using the crystal orientation matrix, they are expressed in the laboratory, sample holder and the sample coordinate systems through changes of basis. Deviatoric strain measurements with errors smaller than 5×10^{-5} were reported for the BM32 setup in optimal conditions (highly perfect germanium single crystal) [36]. In this study, the uncertainties related to deviatoric strains were estimated to be 2×10^{-4}. This only includes

assessments on the parameters used in the analysis software.

To determine the unit cell parameter a and thus the full strain tensor, the energy of at least one Bragg reflection must be measured. Three methods were developed for that purpose: switching from polychromatic mode to tunable-energy monochromatic beam mode [37], using 1D or 2D energy-dispersive detectors [31, 38] and a crystal filter [39] while remaining in the polychromatic mode. In this study, an energy-dispersive point detector was used (see Fig. 2). The advantage of this method is that it does not require any modification of the beamline setup, and it is easily implemented and provides easily interpreted data obtained with counting times around hundreds of seconds. The simulation capabilities of the *LaueTools* software provided the Laue pattern on the sample side and allowed to position the energy-dispersive detector in the axis of diffracted beams. The 150 eV energy resolution of the detector led to an accuracy on reflection energies ΔE of about 5–10 eV. The corresponding uncertainty on the crystal lattice parameter a depends on the energy E of the reflection ($\Delta E/E = \Delta a/a$). With a close to 3.59 Å, Δa is in the $1-3 \times 10^{-3}$ Å range. Therefore, errors in the order of $0.3-0.8 \times 10^{-3}$ are obtained for the diagonal components of the full strain tensor.

The γ phase is a solid solution with a random distribution of the chemical species on a face-centered cubic lattice (see Fig. 4a). The γ' phase corresponds to an ordered face-centered cubic $L1_2$ structure in which the corner of the cubic lattice and the face centers are not equivalent atomic sites (α and β in Fig. 4b). The distribution of atoms consists in chemical elements which occupy preferentially the α or the β sites, like aluminum and nickel, respectively.

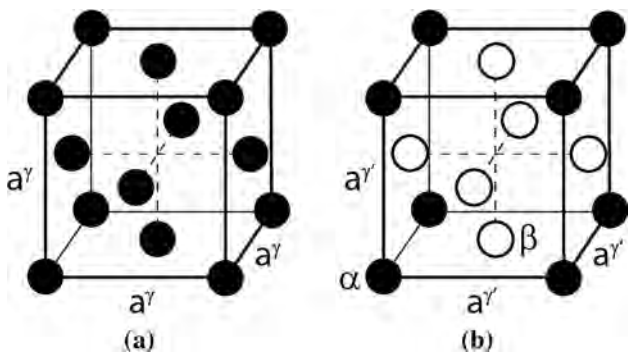

Figure 4 The crystallographic structure of **a** the γ phase (A1), **b** the γ' phase ($L1_2$).

Some occupy indifferently the two sites like titanium. The space group of the γ and the γ' phases are, respectively, $Fm\bar{3}m$ (225) and $Pm\bar{3}m$ (221). In the following, Bragg spots are divided into two categories: those corresponding to fundamental reflections for which the three Miller indices have the same parity and the superstructure reflections with Miller indices of different parities (see Fig. 3). The fundamental reflections are related to the face-centered cubic lattice. Due to the cube–cube orientation relationship between the γ and γ' phases, they correspond to the sum of the intensities diffracted by the two phases and thus provide information associated with the whole irradiated volume. The superstructure reflections are related to the chemical ordering of the face-centered cubic lattice. They are thus only due to the diffraction by the γ' phase.

The unstrained cubic lattice parameters of the γ and γ' phases were measured by Wlodek et al. [29] after chemical etching in an N18 alloy characterized by an average grain size of 10 µm and three populations of γ' precipitates. Although the microstructure investigated here is slightly different, the formation temperature of the secondary γ' precipitates can be assumed to be comparable. Therefore, the strain calculations were performed by considering the following cubic lattice parameter values for, respectively, the γ' phase and the average alloy: $a_0^{\gamma'} = 3.5873$ Å and $a_0^{\gamma+\gamma'} = 3.5917$ Å. The last value was drawn from Vegard's law; it applies to a microstructure with incoherent interfaces between the precipitates and the matrix.

Results

In the following, all the tensor components are expressed in the local cylindrical coordinate system ($\hat{\mathbf{e}}_r$, $\hat{\mathbf{e}}_\theta$, $\hat{\mathbf{e}}_z$) of Fig. 2. Two types of maps are analyzed: (1) large maps recorded with a 50-µm step size to quantify long-range residual strain fields. (2) Fine maps recorded close to the edge of the sample with a 5-µm step size to observe how strain fields are accommodated at the grain scale. Uncertainties are indicated in parentheses. The next section describes the results related to the deviatoric strain tensor components. The results related to the full strain tensor determination are then presented in "Full

strain tensor measurements" section for sake of clarity.

Initial state

Measurements were taken on the sample labeled S1 in Table 2, to quantify the initial deviatoric strain fields caused by the manufacturing process, the grain growth and coherency strains due to the lattice mismatch between the precipitates and the matrix.

Figure 5 represents 3 mm × 1 mm grain orientation and deviatoric elastic strain maps obtained from the fundamental reflections (50-µm map step size). The sample edge is at the left of the maps and the sample center at right. Isoradius contours are represented by the solid lines which have spacings of 100 µm steps. The grain orientation map in Fig. 5a includes 125 grains. The colors are related to the rotation angle between the Cartesian systems of coordinates associated with the crystal lattice and the laboratory (axis-angle representation). Two neighboring pixels were considered in the same grain when the misorientation angle between the crystal lattices was lower than 5°. It is worth mentioning that although the pixel size is 50 µm in maps, the beam size is close to 1 µm. Since the average grain size of the sample is 40 µm, some grains are not represented in the orientation map. The amplitudes of deviatoric strains were lower than 0.5×10^{-3}, except in the 500-µm thick outer layer where they can reach 2×10^{-3} due to the machining (grinding) of the fatigue test specimen. The analysis of superstructure reflections resulted in maps very similar to those of Fig. 5 (see "Appendix 2"). When the strains in the average alloy and in the γ' phase are identical, the same applies for the γ phase, which has a volume fraction close to 50%. Therefore, the measured strains are more representative of the manufacturing process and the grain growth than of coherency stresses caused by the lattice mismatch between the matrix and the precipitates; the latter are hardly detectable using deviatoric strains owing to their cube–cube orientation relationship.

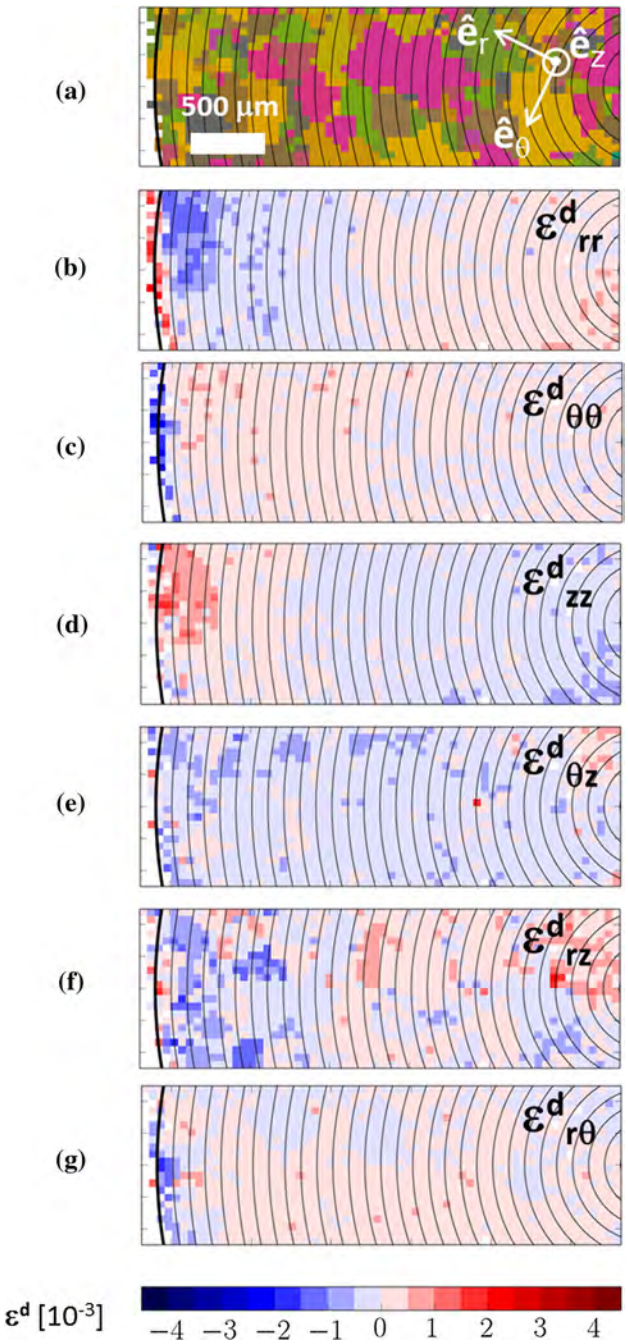

Figure 5 3 mm × 1 mm maps obtained from X-ray microdiffraction measurements with a 50 µm steps size in the untreated sample S1. **a** Grain orientation map. **b**–**g** Average alloy ($\gamma + \gamma'$ phase) deviatoric elastic strain components in the cylindrical coordinate system related to the sample surface represented in **a**. The sample edge is at left of the maps and the sample center at the right. Lines are isoradius contours with 100-µm spacings.

Shot-peened state

Measurements were realized on the cross section of the cylindrical sample labeled S2 in Table 2, whose circumference was uniformly impacted by the steel shots. The radial direction $\hat{\mathbf{e}}_r$ corresponds to the average peening direction and the axial direction $\hat{\mathbf{e}}_z$ is

orientated along the surface normal of the cross section.

Figure 6 represents the grain map and the maps of the six components of the deviatoric strain tensor (in units of 10^{-3}) resulting from the analysis of fundamental reflections in a 5 mm × 2 mm mapping area (50-µm mapping step size). The sample edge corresponds to the thicker contour line on the left-hand side of maps. Arrows indicate the average shot-peening directions. In the 300-µm thick white area close to the sample edge, the crystal lattice underwent high heterogeneous deformation. The diffraction spots were thus spread out (asterism). Their intensity was so weak that it was not possible to separate them from the intensity background due to a too small acquisition time. The determination of the grain orientation and strains was therefore not possible. In comparison with the reference state labeled S1 (Fig. 5), the shot-peening strongly modified the diagonal components of the strain tensor (ε^d_{rr}, $\varepsilon^d_{\theta\theta}$, ε^d_{zz}) and weakly modified the shear components. The latter exhibited variations of positive and negative strains with amplitudes lower than 0.5×10^{-3} in the biggest part of the maps. However, heterogeneous strains with amplitudes larger than 1×10^{-3} were

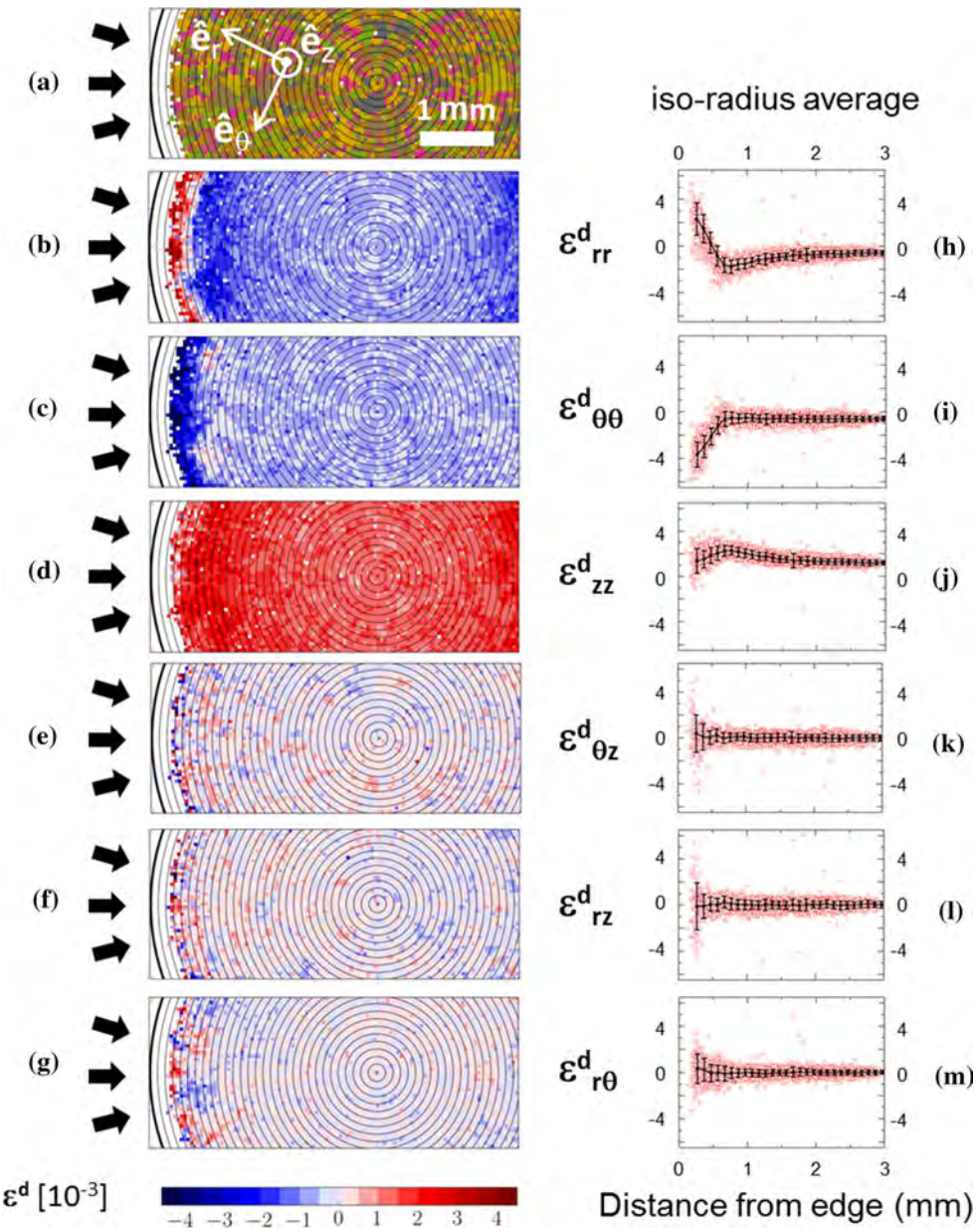

Figure 6 5 mm × 2 mm maps (50-µm step size) obtained from the analysis of fundamental reflections of the shot-peened sample S2. **a** Grain maps and the cylindrical system of coordinates. **b**–**g** Average alloy ($\gamma + \gamma'$ phases) deviatoric elastic strain components. Arrows on the sample edge side indicate the average directions of the shot-peening. **h**–**m** Individual (symbols) and averaged values along the isoradius contour lines (line) spaced every 100 µm. Error bars correspond to standard deviations. Strains are given in units of 10^{-3}.

measured at distances between 300 and 800 µm from the sample edge (see Fig. 6e–g). For the diagonal components, the strain fields were modified in the entire sample and mainly depended on the distance from its center. The average values of deviatoric strains on the isoradius contour lines are represented in Fig. 6 on the right side of maps. The three diagonal components behave differently: ε^d_{rr} is positive in the most external layer and becomes negative after a distance of 400 µm, whereas $\varepsilon^d_{\theta\theta}$ and ε^d_{zz} are, respectively, negative and positive at all distances. The standard deviation is close to 0.5×10^{-3}. The shear strain components are zero on average (Fig. 6k–m) but strong fluctuations between grains (up to $\pm 5 \times 10^{-3}$) are observed up to a distance of approximately 400 µm from the sample edge (Fig. 6e–g).

We now analyze the measurements recorded with a 5-µm step size close to the shot-peened edge of the sample. The 1 mm × 0.25 mm maps representing the grains and the ε^d_{rr}, $\varepsilon^d_{\theta\theta}$ and $\varepsilon^d_{r\theta}$ strain components are shown in Fig. 7. Results for the average alloy ($\gamma + \gamma'$) are on the left-hand side and those for the difference between the average alloy and the γ' phase on the right-hand side. The sample edge is located at left of the figures. For this set of measurements, the acquisition time has been increased to better differentiate the Laue spots from the background signal in the hardened layer. However, due to the asterism, the position of each reflexion was not accurately defined. The intensity profile of the elongated spots was indeed composed of multiple peaks. The least-squared fitting with a regular function (e.g., Gaussian, Lorentzian) yielded uncertainties on the Bragg angle of the order of several tens of mrad. This error related to the position of each Laue spot resulted in uncertainties on the grain orientation of several degrees and unrealistic values of strains. In Fig. 7, only the grain orientation is thus showed in the 300-µm thick layer close to the sample edge (Fig. 7a) and white areas are represented on strain maps. This difficulty is also encountered with the EBSD technique [16, 17]. The general appearance of the strain field for all components was similar to the one described above. At this scale, the analysis clearly reveals the strain heterogeneities within grains and close to the grain boundaries. The strain heterogeneities and the grain microstructure of Fig. 7a are weakly related for the ε^d_{rr} and $\varepsilon^d_{\theta\theta}$ components (Fig. 7b, c) and better related for the $\varepsilon^d_{r\theta}$ shear component (Fig. 7d). The analysis of the Laue patterns associated with the γ' phase showed that the strain fields were very similar to those in the average alloy. As shown in Fig. 7e–g, which represents the difference between the two strain fields for the ε^d_{rr}, $\varepsilon^d_{\theta\theta}$, and $\varepsilon^d_{r\theta}$ components, some significant deviations are

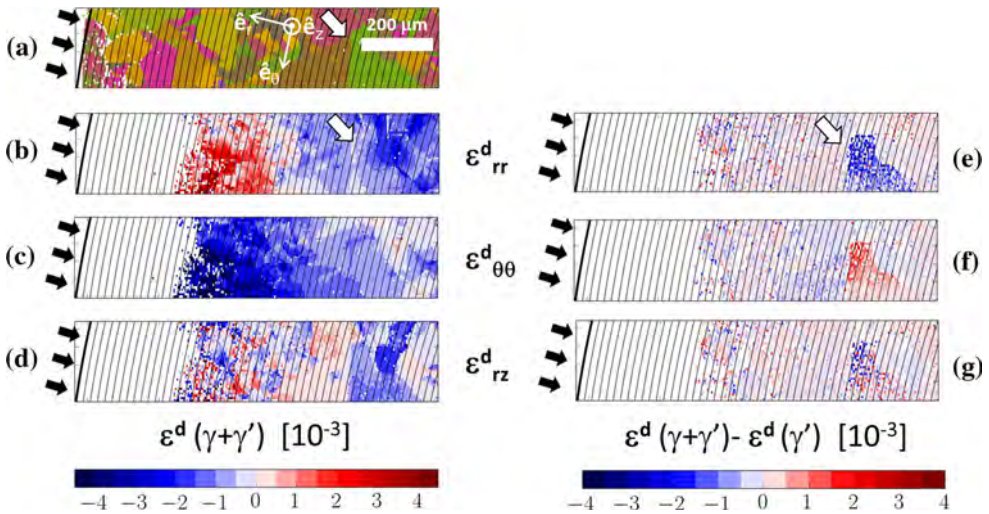

Figure 7 1 mm × 0.25 mm maps (5-µm step size) related to the shot-peening sample (S2). **a** Grain orientation. **b**–**d** Deviatoric strain components obtained from the analysis of fundamental reflections ($\gamma + \gamma'$ phases). **e**–**g** Differences between strains related to the average alloy and strains related to the γ' phase. The sample edge is located at the left side of figures. Arrows indicate the average shot-peening direction. The strain components are given with respect to the cylindrical coordinate system ($\hat{\mathbf{e}}_r$,$\hat{\mathbf{e}}_\theta$,$\hat{\mathbf{e}}_z$) represented in **a**. Lines are isoradius contours with a spacing of 20 µm.

measured in a specific grain indicated by arrows on the maps.

Strain redistribution after an isothermal holding

The redistribution of deviatoric strains caused by the shot-peening was characterized after a 1 h 40 min hold at 450°C (sample labeled S3 in Table 2). This temperature was representative of the thermal conditions endured by the inner part of high-pressure turbine disks (bore area) [40, 41].

After the heat treatment, the dependence of strain fields on the distance from the sample center was again observed in large and fine maps. The highly deformed layer was also observed close to the sample edge (white areas). The behavior of the strain components was similar to those represented in Figs. 6 and 7 for the shot-peened sample S2 (see maps in "Appendix 3"). The main differences consisted in the presence of some accurate data in the hardened layer reflecting restoration effects (shown in Fig. 16), of lower strain levels and higher strain fluctuations. The last two effects are evidenced in Fig. 8, which represents the six independent components of the deviatoric strain tensor obtained from the large maps as a function of the distance from the sample edge. For sake of comparison, the average profiles obtained in Fig. 6 for the shot-peened sample S2 are represented by the black lines. As for the shot-peened sample S2 (Fig. 7), the analysis of superstructure reflections (γ' phase) in the Laue patterns of sample S3 led to strain levels quite close to those obtained for the average alloy (not shown).

Strain redistribution after fatigue

The solicitation axis matches the $\hat{\mathbf{e}}_z$ direction of the cylindrical coordinate system used to express strain components (see Fig. 2). The fatigue conditions described in detail in "Appendix 1" correspond to a regime where a net plastic strain is accumulated during cycles, which consist of repeated tensile deformations. Assuming that strains introduced by shot-peening may have fully relaxed at failure, the fatigue test was interrupted after 300 cycles (1 h 40 min, approximately 25% of the lifetime [4]) at zero applied stress. To better verify the interaction of strain fields arising from shot-peening and fatigue, a sample subjected to fatigue only was also characterized using μXRD.

Figure 9 represents 3 mm × 1 mm maps showing the grains and the deviatoric strain components related to the average alloy. Figures related to the shot-peened sample S4 are at left of the figures and those related to the sample S5 only fatigued are at right. For the shot-peened sample, only a few characteristics of the strain maps of Fig. 6 are observed after fatigue at 450°C (Fig. 9b–g): the 300-μm thick white areas and the average strain behavior of the neighboring shell located between 300 and 800 μm from the sample edge. For all components, large strain heterogeneities were observed in the rest of the maps with amplitudes in the range $\pm 2 \times 10^{-3}$; they average to zero. The underlying grain microstructure was not identifiable in strain maps because some positive and negative strains occur from one pixel to the other. This means that heterogeneous intragranular deformation takes place in the material. Interestingly, no trace of the load direction ($\hat{\mathbf{e}}_z$) was found in the residual elastic maps. The strain fields related to the sample S5 which, was only subjected to fatigue (Fig. 9i–n), differ significantly from those measured in the sample S4 (Fig. 9b–g). The ε^d_{zz} component which corresponds to the load axis was close to -1×10^{-3} regardless of the distance. The ε^d_{rr} and ε^d_{rz} components also display nonzero elastic strains regardless of the distance. Such behavior was similarly observed during an uniaxial tensile test in a nickel-based alloy [42].

The fine maps recorded on the sample edges of the shot-peened and fatigued sample S4 revealed weak modifications of the surface layer with respect to the shot-peened sample S2. The strain amplitudes, the thickness of the hardened layer were similar. Only some restoration effects occurred in the hardened layer (white areas) due to the temperature (see Fig. 17 in "Appendix 4").

Full strain tensor measurements

Energy measurements were taken at different sample positions with the point detector located on the sample side (see Fig. 2). The energy, the Miller indices and the Bragg angle of selected reflections were used to determine the missing scaling factor in the analysis of the Laue pattern. This allowed to

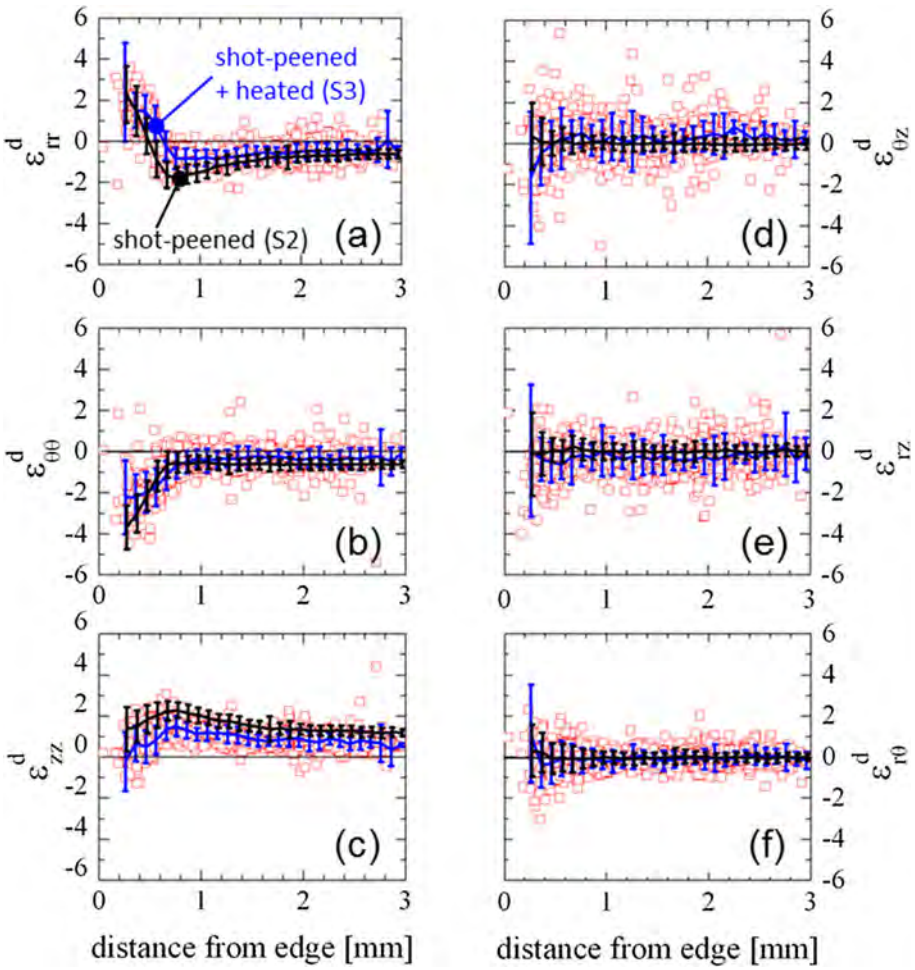

Figure 8 Deviatoric elastic strain components of the average alloy as a function of the distance from the sample edge after the shot-peening operation and isothermal holding at 450°C for 1 h 40 min (S3). The blue solid lines correspond to averages on isoradius, error bars to standard deviations and red square symbols to individual values. The average profiles of Fig. 6 related to the shot-peened sample S2 are represented by the black lines.

determine the full elastic strain tensor components. In principle, for each sample position, at least one fundamental and one superstructure reflection were searched within the translation range of the detector to determine the strain components related, respectively, to the average alloy ($\gamma + \gamma'$) and to the γ' phase. However, in practice, two limitations were encountered: (1) both reflections could not be reached, and (2) the energies of the reflections were superimposed to fluorescence energies of the chemical elements. For some sample positions, the energy of only one reflection was therefore determined.

Initial state

Conventional Laue diffraction measurements in a grain located at the center of the sample led to the following deviatoric elastic strain tensors for the average alloy ($\gamma + \gamma'$) and the γ' phase:

$$\varepsilon^{d}_{\gamma+\gamma'}[10^{-3}] = \begin{pmatrix} 0.2(2) & -0.3(2) & 0.1(2) \\ -0.3(2) & 0.1(2) & -0.8(2) \\ 0.1(2) & -0.8(2) & -0.3(2) \end{pmatrix}_{(\hat{\mathbf{e}}_r,\hat{\mathbf{e}}_\theta,\hat{\mathbf{e}}_z)} \quad (1)$$

$$\varepsilon^{d}_{\gamma'}[10^{-3}] = \begin{pmatrix} 0.3(2) & -0.3(2) & 0.1(2) \\ -0.3(2) & 0.4(2) & -0.8(2) \\ 0.1(2) & -0.8(2) & -0.7(2) \end{pmatrix}_{(\hat{\mathbf{e}}_r,\hat{\mathbf{e}}_\theta,\hat{\mathbf{e}}_z)} \quad (2)$$

Deviatoric components are close to zero for the two tensors. The measured energy of the $31\bar{5}$ (fundamental) and $31\bar{6}$ (superstructure) reflections were, respectively, 13416(4) eV and 16442(5) eV. This permits to calculate the full strain tensors:

$$\varepsilon^{full}_{\gamma+\gamma'}[10^{-3}] = \begin{pmatrix} 1.2(3) & -0.3(2) & 0.1(2) \\ -0.3(2) & 1.1(3) & -0.8(2) \\ 0.1(2) & -0.8(2) & 0.8(3) \end{pmatrix}_{(\hat{\mathbf{e}}_r,\hat{\mathbf{e}}_\theta,\hat{\mathbf{e}}_z)} \quad (3)$$

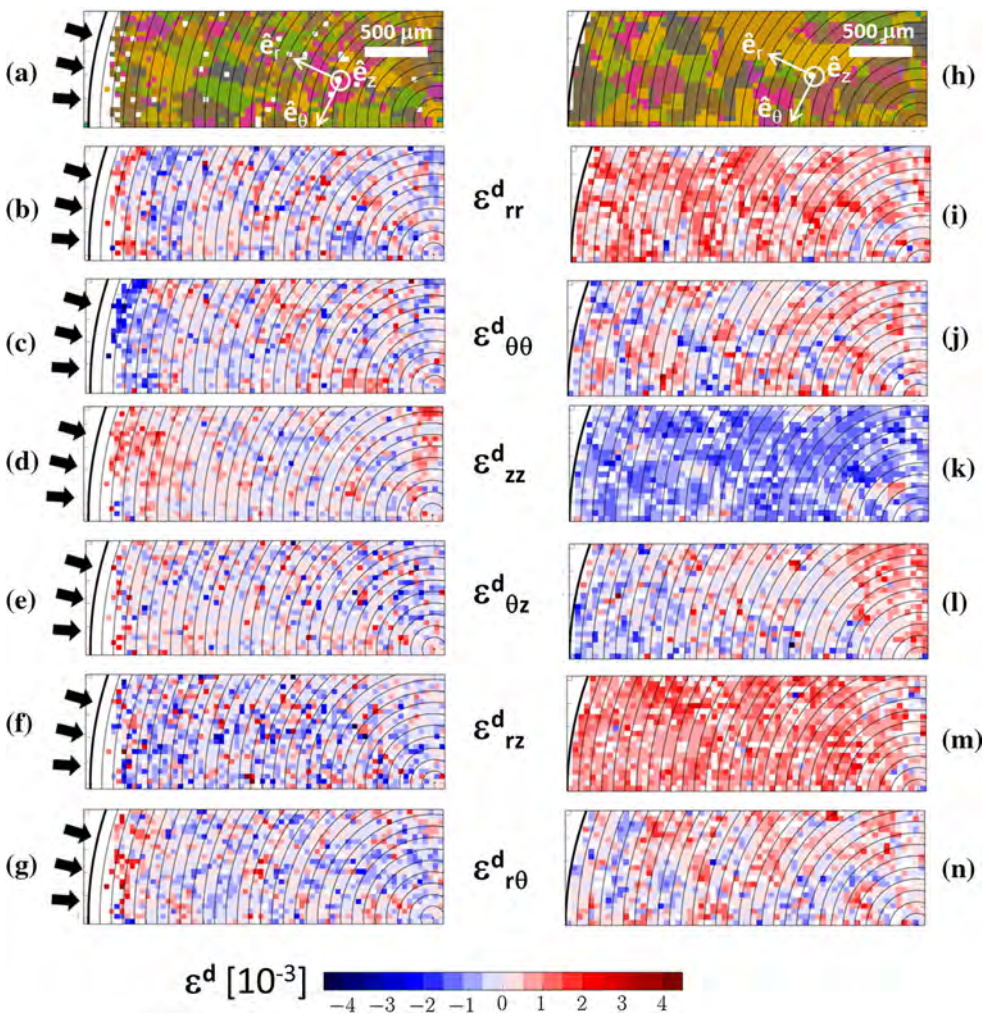

Figure 9 3 mm × 1 mm (50-µm step size) grain orientation and deviatoric strain maps (average alloy) in, **a**–**g** sample S4 subjected to shot-peening followed by 300 cycles of fatigue at 450°C, **h**–**n** sample S5 subjected to 300 cycles of fatigue at 450°C. The sample edge is located at the left of the figures. Arrows indicate the average peening directions and lines with 100-µm spacing are isoradius contours.

$$\varepsilon^{full}_{\gamma'}\,[10^{-3}] = \begin{pmatrix} -0.1(3) & -0.3(2) & 0.1(2) \\ -0.3(2) & -0.2(3) & -0.8(2) \\ 0.1(2) & -0.8(2) & -0.4(3) \end{pmatrix}_{(\hat{\mathbf{e}}_r,\hat{\mathbf{e}}_\theta,\hat{\mathbf{e}}_z)} \quad (4)$$

For the γ' phase, the full and deviatoric strain tensors were very close to each other. For the average alloy, the hydrostatic part (Tr $\varepsilon^{full}/3$) was $1.0(3) \times 10^{-3}$. This means that most of the strains related to the diagonal components of the average alloy were caused by the γ phase. Further measurements in different grains showed that the amplitudes of deviatoric strains were below 1×10^{-3} for the two phases and that hydrostatic strains up to 2×10^{-3} can be also reached in the γ' phase.

Shot-peened state

Figure 10a–c represents the *a*, *b* and *c* lattice parameters of the crystal unit cell as a function of the distance from the shot-peened edge of the sample. Open symbols correspond to the γ' phase and closed symbols to the average alloy ($\gamma + \gamma'$). For the two sample positions labeled "1" and "2", the energy of a superstructure and a fundamental reflection were measured. We observed that the crystal parameters were quite similar, showing that the coherency of the γ and the γ' phases was not affected by the shot-peening operation. For some sample positions, lattice parameters were calculated from two reflections of the same type (fundamental or superstructure). The accuracy on the lattice parameter values was of the order of $1-2 \times 10^{-3}$Å. The fluctuations of the lattice parameter values with respect to the strain-free lattice parameters were due to the presence of residual strains and to the different crystal lattice orientations with respect to the peening direction. The full strain profile calculated from the lattice parameters and the crystal orientations is represented in Fig. 10d–f. Only diagonal components are shown because deviatoric

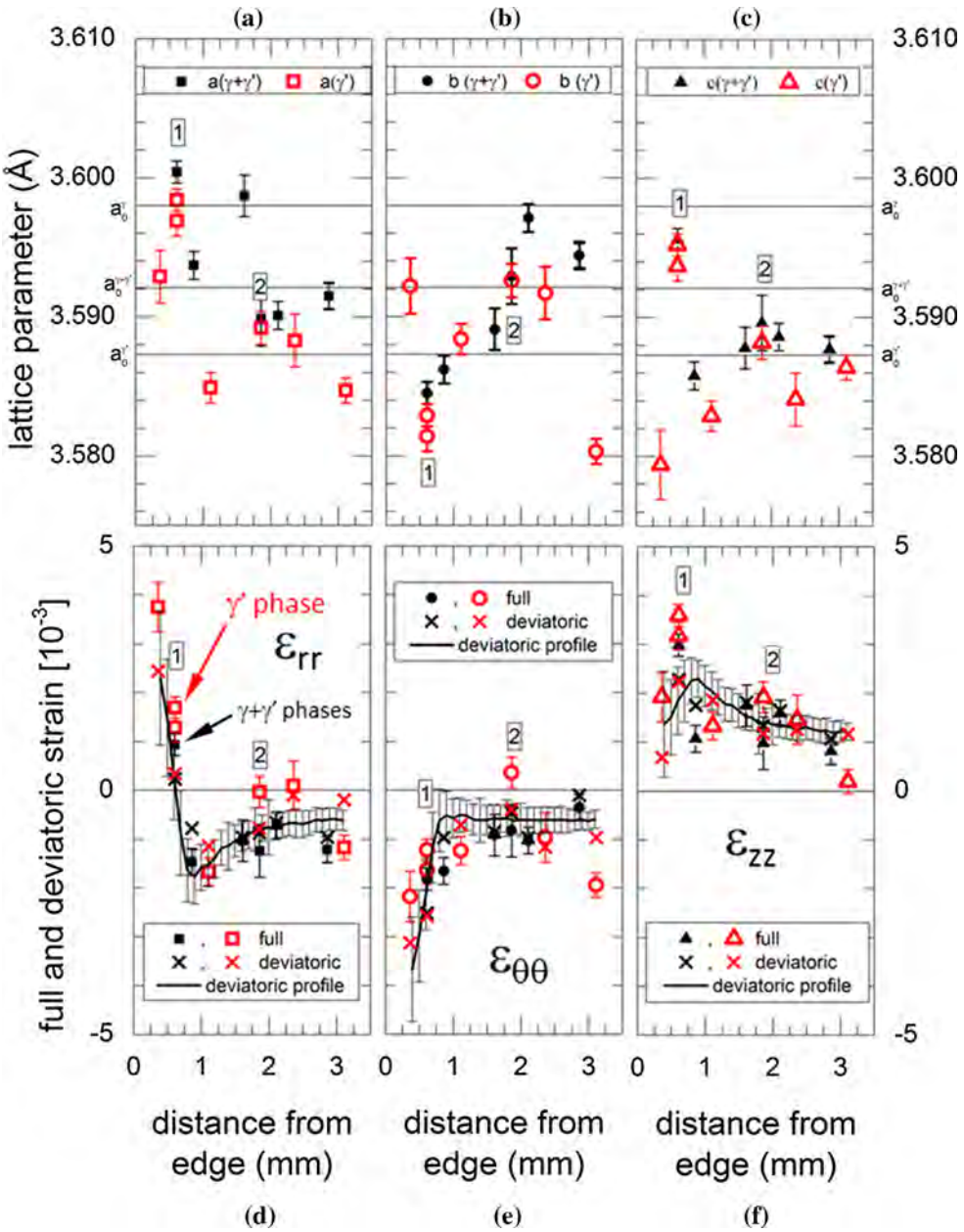

Figure 10 **a–c** Crystal unit cell parameters for the average alloy (closed symbols) and the γ' phase (open symbols) as a function of the distance from the shot-peened edge of the sample S2. Horizontal lines correspond to the strain-free lattice parameter values of the average alloy, the γ and the γ' phases [29]. **d–f** Full and deviatoric strain components $\varepsilon_{rr}, \varepsilon_{\theta\theta}$ and ε_{zz}. The symbols correspond to the values obtained from energy measurements, open for the γ' phase and closed for the average alloy ($\gamma + \gamma'$). The line and errors bars are, respectively, the average deviatoric strain and the standard deviations obtained from the maps in Fig. 6 (see text for detail).

and full strain components are mathematically equal for non-diagonal terms (see e.g., Eqs. 3 and 4). The strain behavior was similar for the γ' phase (open symbols) and the average alloy (closed symbols). For distances larger than 1 mm, strain amplitudes were lower than 2×10^{-3}. For the two labeled sample positions, the difference of strain between the average alloy and the γ' phase was lower than 1.5×10^{-3}. For $d = 0.25$ and $d = 0.5$ mm, larger strain were measured for both the average alloy and the γ' phase.

In Fig. 10d–f, the cross symbols correspond to the deviatoric strain values obtained from the full strain measurements. For a given distance from the sample edge, Laue patterns from only one sample position were analyzed. For sake of comparison, the average deviatoric strain profile obtained from the deviatoric maps of Fig. 6 is also represented in Fig. 10d–f. (black line and standard deviation bars). The deviatoric strain values obtained from the full strain measurements (crosses) are very close to those obtained from the strain maps (black line). This shows that the data related to investigated sample positions are representative of the average behavior described in "Shot-peened state" section. We observe that the behavior

of the full and deviatoric components are roughly similar. They differ by less than $1-2\times10^{-3}$. ε_{rr} is positive and becomes negative after about 0.5 mm from the sample edge, whereas $\varepsilon_{\theta\theta}$ and ε_{zz} are, respectively, negative and positive at all distances.

Shot-peened and fatigued state

The diagonal components of the full strain tensor obtained from energy measurements for the sample S4 subjected to shot-peening and fatigue at 450°C are represented in Fig. 11 for the average alloy (closed symbols) and the γ' phase (open symbols). As in the previous section, the solid line corresponds to the averaged deviatoric strains taken from isoradius contours of Fig. 9b–d. Fatigue has mostly removed the effects introduced by the shot-peening (see Fig. 10). Indeed, all components behave in a similar manner with full strain amplitudes fluctuating between -2×10^{-3} and 2×10^{-3}. In the investigated grains, the strain of the γ' phase was very close to that of the average alloy. Such behavior could also have been attributed to a reference sample, which has not been subjected to shot-peening and/or fatigue. Finally, even if only one full strain value was measured in the hardened layer (white areas in deviatoric maps), the fact that measured strains did relax deeper into the material suggests that the residual strains in the hardened layer were also significantly relaxed for elastic equilibrium reasons. This was observed, for example, in the residual stress profiles measured in a shot-peened IN100 superalloy subjected to different thermal and mechanical loadings [9].

Discussion

Deviatoric stresses and crystal misorientations

To estimate residual stresses from measured strains, single-crystal elastic moduli should be known for each phase. This implies the manufacturing of a specific single crystal and in situ mechanical tests. Such work is out of the scope of this study. In this article, the Voigt and Reuss relationships between the macroscopic effective elastic constants of the material (Young modulus and Poisson's ratio) and the elastic constants of the cubic single crystal were used (see detail in "Appendix 5"). The difference between the Voigt and Reuss averaging methods is of the order of 10 MPa in the crystal coordinate system and the 2×10^{-4} uncertainty on strains is equivalent to a 40 MPa uncertainty on stresses. Therefore, only the Voigt approximation was taken into account for the stress calculation. In our measurements, deviatoric strain fields were identical for the average alloy and the γ'

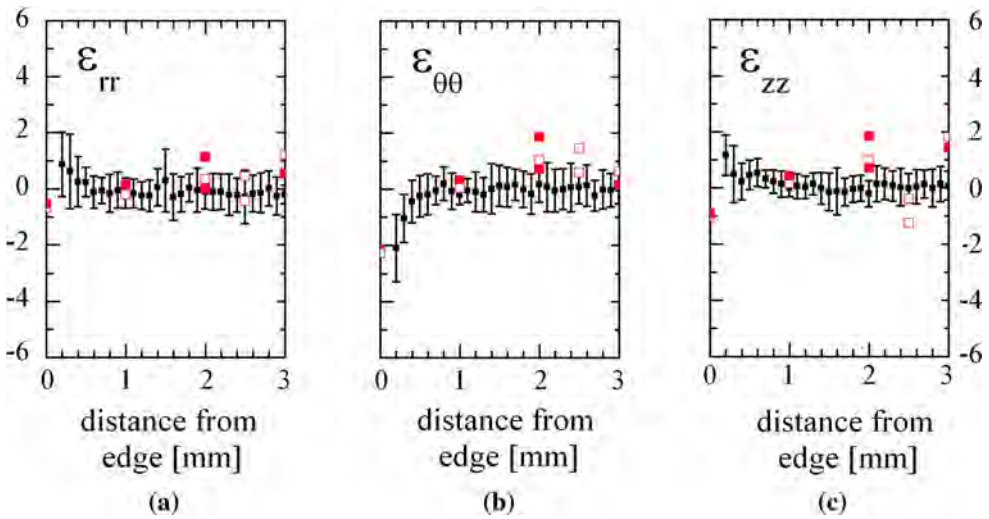

Figure 11 Deviatoric elastic strain components in 10^{-3} units as a function of the distance from the sample edge after shot-peening and 300 cycles of fatigue at 450° (S4). The solid lines correspond to averages of isoradius lines and error bars to standard deviations obtained from the large maps of Fig. 9b–d. Square symbols correspond to data obtained with energy measurements: the average alloy (closed symbols) and the γ' phase (open symbols).

phase. Because the γ' volume faction was close to 50%, the deviatoric strain fields of the γ and γ' phases were similar. Only differences in elastic constants would result in differences in deviatoric stresses. Figure 12 summarizes the behavior of the three diagonal deviatoric components (σ^d_{rr}, $\sigma^d_{\theta\theta}$, σ^d_{zz}) and of a shear component ($\sigma^d_{r\theta}$) for each investigated mechanical state of the N18 superalloy. The color scale ranges from −1000 to 1000 MPa; the latter value is the measured yield strength of our samples at room temperature. Deviatoric stresses follow the same trends as the corresponding deviatoric strains: negative (positive) strains lead to compressive (tensile) stresses, respectively. The quantitative results clearly show the effect of shot-peening on the reference state as well as the effects of the applied thermal and mechanical loadings. Even if low stress amplitudes occur in the inner part of samples, the sensitivity of the Laue microdiffraction technique (about 50 MPa) was large enough to reveal differences between each state in terms of stress amplitudes and stress heterogeneities. It is worth mentioning that the stress components in Fig. 12 are related to the deviatoric stress tensor. In all generality, the behavior of the stress field related to the deviatoric tensor σ^d differs from the one related to the full tensor σ because of the relationship between their components: $\sigma^d_{ij} = \sigma_{ij} - \frac{1}{3}\mathrm{Tr}\,\sigma\,(i,j = r,\theta,z)$. Microhardness tests were performed from the sample edge to 1 mm for each shot-peened state (S2, S3, S4). No differences were observed upon overlapping the profiles. The Vickers hardness linearly decreases from 650 to 460 HV at $d = 0.5$ mm and then is constant.

The kernel average misorientation (KAM) in the EBSD/SEM is often used to estimate the plastic strain induced by surface treatments or mechanical loading conditions. The angular resolution for conventional and high-resolution analyses is, respectively, 0.1°−1° and 0.01° [43, 44]. With the μXRD technique, the resolution is close to 0.01° [39]. For the reference sample (S1), the KAM is lower than 0.02°, except in the 100-μm thick external layer, where misorientations are in the range of $0.3° - 0.5°$ owing to the machining operation (not shown). Figure 13 represents KAM maps calculated from μXRD measurements with a 5-μm step size, for the shot-peened (S2), the shot-peened and heated (S3), the shot-peened and fatigued (S4) and the fatigued (S5) states. On the left of the figure, the angular resolution is 0.1°, which is similar to the better accuracy reachable with conventional EBSD. On the right side, the resolution is 0.02°, which corresponds to the accuracy of our measurements. This value is also similar to the HR-EBSD resolution. Isoradius contour lines have a spacing of 100 μm. The dotted line separates the inner layer of the samples, in which the microhardness is constant (460 HV), from the external hardened layer in which the hardness linearly increases from 460 to 650 HV. Blue lines which are superimposed on maps represent the grain boundaries. Figure 13a–d shows that, with the exception of the 500-μm thick layer affected by the shot-peening close to the sample edge, misorientations were mostly localized in the vicinity of the grain boundaries. When comparing Fig. 13a, c, it can be observed that fatigue did not introduce additional misorientations at 1 mm from the edge (bottom of the figures). This is similar to the EBSD

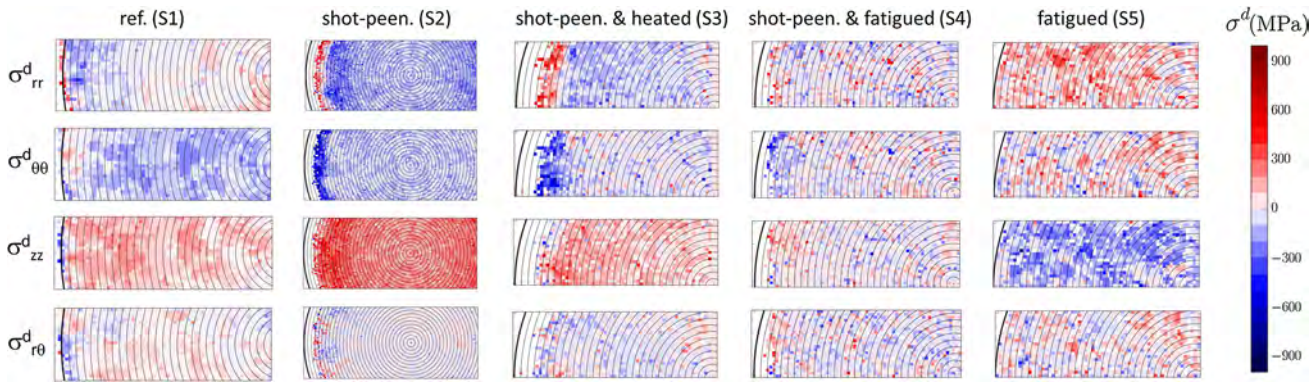

Figure 12 Maps of deviatoric stress tensor components (σ^d_{rr}, $\sigma^d_{\theta\theta}$, σ^d_{zz} and $\sigma^d_{r\theta}$) calculated from measured strains (50-μm step size) in the reference (S1), shot-peened (S2), shot-peened and heated (S3), shot-peened and fatigued (S4) and only-fatigued (S5) samples. The sample edge is localized at the left of the figures. Isoradius contour lines are represented with a spacing of 100 μm.

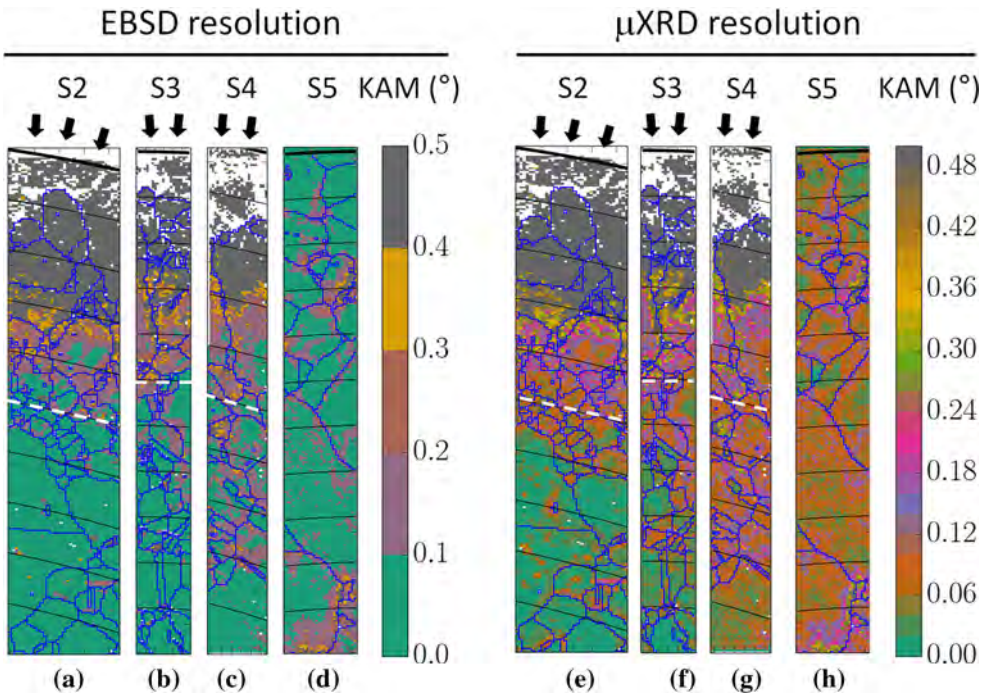

Figure 13 KAM maps (5-μm step size) in the 0°−0.5° range for the shot-peened (S2), shot-peened and heated (S3), shot-peened and fatigued (S4) and fatigued (S5) states (see Table 2). In **a**–**d** a 0.1° step (EBSD resolution) is used and in **e**–**h** a 0.02° step (μXRD resolution) is used. The sample edge is localized at the top of the figures. Arrows indicate the shot-peened edge of the samples. The grain boundaries are superimposed on the misorientation maps and represented by the blue lines. Isoradius contour lines have a 100-μm spacing.

observations reported in a shot-peened RR1000 superalloy also fatigued at 300°C for 520000 cycles [17]. When the angular resolution is set to 0.02°, the shot-peened state (S2, Fig. 13e) is characterized by three layers: one highly deformed 300-μm thick layer close to the sample edge, then a 300-μm thick layer with intragranular misorientations and in the inner part, a 400-μm thick layer where crystal misorientations were localized mostly in the vicinity of the grain boundaries. If KAM maps are used to quantify the effect of the shot-peening operation [15, 16], the affected depth may therefore vary with the used angular resolution. Here, a difference of 100 μm was observed between 0.1° and 0.02°. In addition to the fact that the three methods are not sensitive to the same physical quantities, this could also explain the differences observed when comparing results from Vickers microhardness, XRD peak width and KAM or GOS measurements in EBSD/SEM. For the sample that was subjected to fatigue only (Fig. 13f), misorientations take place in grains and close to the grain boundaries when the angular resolution is set to 0.02°. This contrasts with the angular resolution of 0.1° (Fig. 13c) which suggests that LCF causes misorientations at only few grain boundaries. Finally, the effect of fatigue on the initial shot-peened state was also better distinguished with a 0.02° resolution (S4, Fig. 13g).

Full stresses

In this study, an energy-dispersive point detector was used to determine the energy of Bragg reflections and further to determine the full stress tensor components without any analytical assumption. This was done from the fundamental reflections related to the average alloy and from the superstructure reflections related to the γ phase. Due to the 150 eV resolution of the detector, the accuracy on Bragg spot energies was close to 10 eV. Then uncertainties on the diagonal components of the strain and stress tensors were, respectively, close to 1×10^{-3} and 250 MPa. For Ni-based superalloys, these values are too high to obtain quantitative data in areas where stresses are expected to be small that is, outside the hardened layer. Unfortunately, in this layer, the asterism of Bragg spots was too large and the determination of stresses was not possible. The fact that it was difficult to measure the energy of a fundamental and a superstructure reflections at each sample position was also an important limitation of the method. The "Rainbow" technique [39] would be a good alternative because energy resolutions of 1 eV may be obtained for the two types of reflection at every sample position [45]. Concerning, a better characterization of the hardened layer, a depth resolution is required in order to have workable outcomes. The differential

aperture X-ray microscopy (DAXM) could help to reach this objective [33].

Conclusions

The residual elastic strain field caused by the shot-peening of the N18 polycrystalline nickel-based superalloy was characterized at the grain scale and at the millimeter scale using the X-ray Laue microdiffraction technique coupled to energy measurements. The deviatoric elastic strain field clearly exhibits the trace of the peening operation in the whole sample cross section. The sensitivity of the Laue microdiffraction method was large enough to quantitatively characterize the crystal misorientations and the deviatoric strain redistribution after an isothermal treatment and a LCF fatigue test both at 450°C for the average alloy and the γ' phase. This is the major result of this article. Although strains in the hardened layer were not accurately quantified owing to strong crystal deformations, our measurements revealed that the deviatoric strain fields remaining after fatigue are not equivalent in an only-fatigued sample and in a shot-peened sample. Strains sensitive to the grain microstructure and to the load direction develop in the first case, whereas in the latter case, large heterogenous intragranular strains occur in a similar manner in all the strain tensor components. We also showed that the depth affected by shot-peening or the effects of the fatigue on the grain scale significantly differ depending upon the angular resolution used in KAM calculations (0.1° or 0.02°). In our measurements, only the KAM map can provide quantitative data in the 300-μm thick hardened layer produced by shot-peening.

This study also showed that the fast mapping capabilities of the Laue technique associated with the latest development of Bragg reflection energy measurements, is suitable for providing useful quantitative data for the residual stress determination in microstructures whose grain size is too large to use the $\sin^2\psi$ method or too small to use the Ortner's approach. The obtained micro- and macrodeviatoric strains, determined with an accuracy close to 2×10^{-4}, can be confronted to HR-EBSD or FIB-DIC measurements, to modeling at the grain scale (e.g., crystal plasticity or dislocation dynamics approaches) or at the mesoscopic scale (finite element-based approaches) [46]. Concerning the full strain measurements, the results obtained for the reference, the shot-peened and the fatigued states suffered from the 150 eV resolution of the detector, which led to uncertainties close to 1×10^{-3} and 250 MPa on strain and stress values, respectively. The small translation range of the detector and the large number of fluorescence emissions in the energy spectrum make difficult to measure the energy of a fundamental and a superstructure reflection at a fixed sample position. The use of the "Rainbow" technique should improve these two limitations. The accuracy on the full stress tensor components obtained from the energy measurements was not good enough to extract a full stress profile on the cross section of the shot-peened sample. Therefore, it was not possible to quantify surface effects introduced by the cutting of the fatigue specimen on the residual stress components. However, for this purpose, the measured deviatoric stress profiles could be compared (1) to those obtained from full stress measurements on the shot-peened surface using the $\sin^2\psi$ method on a 500 μm depth or (2) to the results of a finite element modeling in which stress relaxations caused by the cutting of the gauge can be simulated. Finally, a quantitative characterization of the hardened layer was not possible because a depth resolution is required in the analysis of the Laue patterns. The differential aperture X-ray microscopy coupled to the Laue microdiffraction technique should be able to overcome this difficulty.

Acknowledgements

This work benefited from the support of the REMEDDIES project (ANR-13-BS09-016) of the French National Research Agency (ANR) and the French Aeronautical and Space Research Foundation (FRAE). The synchrotron data used in this article were collected during ESRF experiments MA3096, 32-02 778 and IN995. Authors gratefully acknowledge the BM32 staff for helpful discussions and technical support, as well as D. Locq, C. Liard and P. Kanouté from ONERA for the alloy development and mechanical testing.

Compliance with ethical standards

Conflict of interest The authors declare that they have no conflict of interest.

Appendix 1: Fatigue testing

Fatigue tests were conducted under strain control with a 100 kN MTS 810 servo-hydraulic testing machine equipped with a split three-zone resistance furnace. Strains were determined with a 12-mm gage length extensometer attached on cylindrical specimen with a diameter of 6.22 mm. A 25°C/min ramp was applied to reach 450°C. The repeated low-cycle fatigue test was then realized with a triangular waveform defined by a 1 Hz frequency, a $10^{-3}\,s^{-1}$ strain rate, a 0 strain ratio ($R_\varepsilon = \varepsilon_{min}/\varepsilon_{max}$) and a 0.5% strain amplitude ($\Delta\varepsilon/2 = (\varepsilon_{max} - \varepsilon_{min})/2$). The stress–strain curve with the first (dashed line) and the 300th (solid line) cycles is shown in Fig. 14.

Appendix 2: Deviatoric elastic strain components associated with the γ' phase in the reference sample S1

Figure 15 is obtained from the analysis of superstructure reflections (Miller indices with different parities) in the Laue patterns recorded in the reference sample. The orientation map and the strain components are related to the γ' phase. In comparison with Fig. 5, similar strain levels are observed. The larger fluctuations in the results arise from the fact that a smaller number of indexed Bragg spots are included in the analysis.

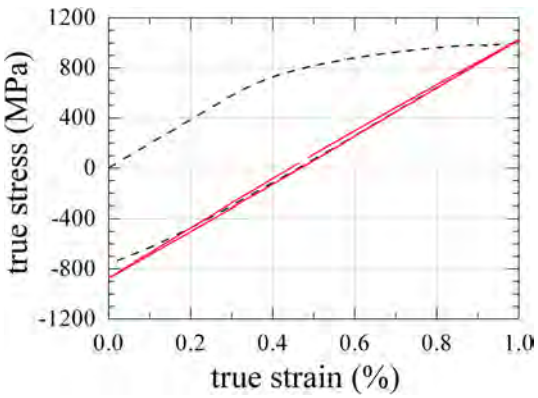

Figure 14 Stress–strain curve corresponding to the interrupted fatigue tests performed at 450°C in the coarse-grained, shot-peened N18 superalloy with a 200 nm average size for the secondary γ' precipitates (no tertiary). The first load cycle is represented by the dashed line and the 300th cycle by the solid line (see S4 in Table 2).

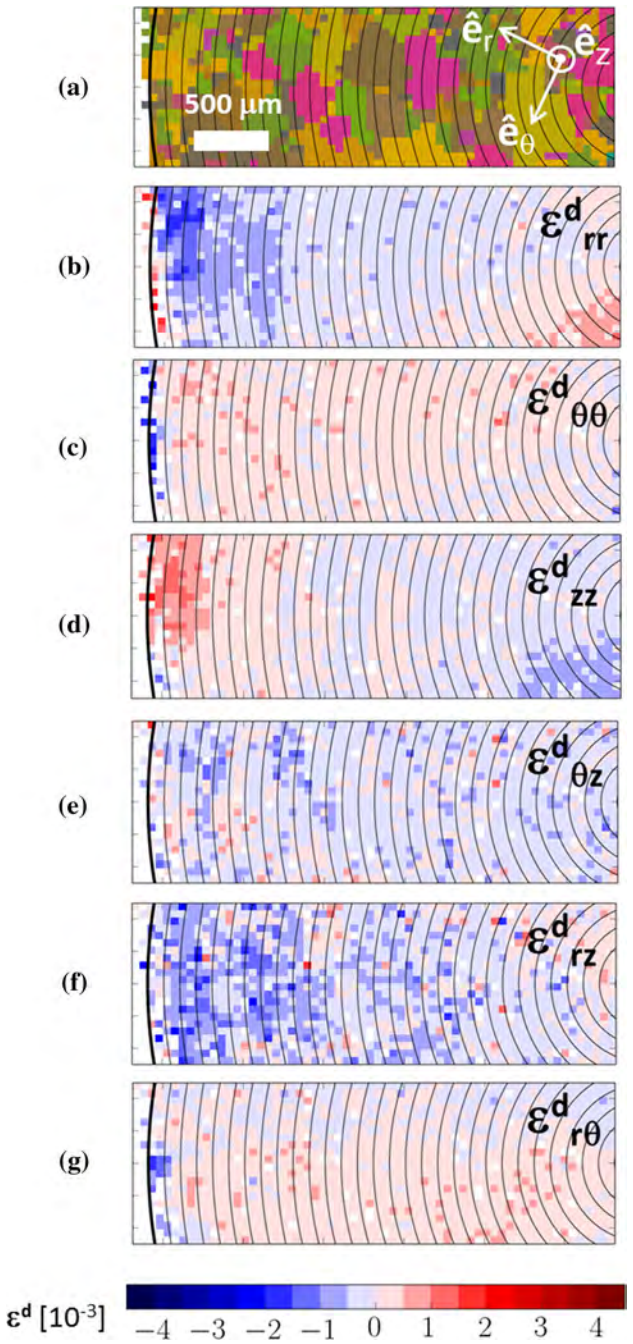

Figure 15 3 mm × 1 mm maps obtained from X-ray microdiffraction measurements using a 50-µm step size in the untreated sample S1. **a** Grain orientation. **b**–**g** Deviatoric elastic strain components associated with the γ' phase (Voigt model) in the cylindrical coordinate system related to the sample surface represented in **a**. The sample edge is at the left side of the maps and the sample center at the right side. The lines are isoradius contours with a spacing of 100 µm.

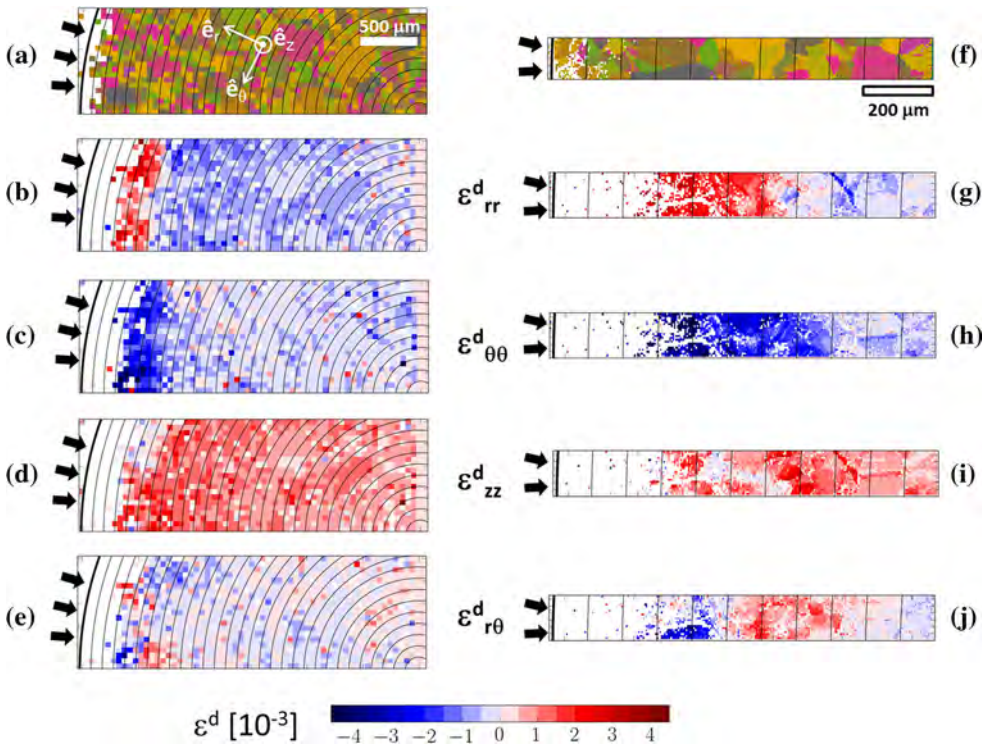

Figure 16 Grain orientation and deviatoric elastic strain maps associated with the shot-peened and heated sample S3. Strain components are represented in the cylindrical coordinate system ($\hat{\mathbf{e}}_r$, $\hat{\mathbf{e}}_\theta$, $\hat{\mathbf{e}}_z$) related to the sample surface and correspond to the average alloy ($\gamma + \gamma'$ phases). The sample edge is located at the left-hand side of the figures. Arrows indicate the average direction of the shot-peening. The isoradius contour lines are spaced every 100 µm. **a**–**e** 3 mm × 1 mm maps recorded with a 50-µm step size. **f**–**j** 1.1 mm × 0.1 mm maps recorded close to the sample edge with a 5-µm step size.

Appendix 3: Deviatoric elastic strain components associated with the sample S3 subjected to shot-peening and heating at 450°C

Figure 16 is obtained from the analysis of fundamental reflections (Miller indices with the same parity) in the Laue patterns recorded in the shot-peened and heated sample S3. Grain orientation and deviatoric strain maps recorded with a step size of 50 µm are at the left of the figure, and those recorded close to the sample edge with a 5-µm step size are at the right side.

Appendix 4: Deviatoric elastic strain components associated with the samples S4 and S5 subjected to fatigue at 450°C

Figure 17 is obtained from the analysis of fundamental reflections (Miller indices with the same parity) in the Laue patterns recorded in the shot-peened and fatigued sample (S4) and in the only-fatigued sample (S5).

Appendix 5: Relationships between the cubic crystal elastic constants and the effective isotropic elastic constants of the related polycrystal

The macroscopic effective elastic constants are found by averaging the anisotropic elastic properties of the individual crystal over all its possible orientations. In the so-called Voigt [47] and Reuss [48] approximations, the elasticity tensor and its inverse are averaged. For a cubic crystal symmetry, this leads to the following expressions for the Young modulus E, Poisson's ratio ν and shear modulus μ of the polycrystal:

$$\begin{cases} E_V = \dfrac{(C_{11}-C_{12}+3C_{44})(C_{11}+2C_{12})}{2C_{11}+3C_{12}+C_{14}} & E_R = \dfrac{5}{3S_{11}+2S_{12}+S_{44}} \\ \nu_V = -\dfrac{C_{11}+4C_{12}-2C_{44}}{4C_{11}+6C_{12}+2C_{44}} & \nu_R = -\dfrac{2S_{11}+8S_{12}-S_{44}}{6S_{11}+4S_{12}+2S_{44}} \\ \mu_V = \dfrac{C_{11}-C_{12}+3C_{44}}{5} & \mu_R = \dfrac{5}{4S_{11}-4S_{12}+3S_{44}} \end{cases} \tag{5}$$

where V and R denote the Voigt and Reuss averaging methods. $\{C_{ij}\}$ and $\{S_{ij}\}$ are, respectively, the three elastic constants and compliances (in Voigt notation) of the cubic crystal. The Zener ratio A, which quantifies the elastic anisotropy, is defined by $2C_{44}/(C_{11}-C_{12})$. If we require that E, ν and A are

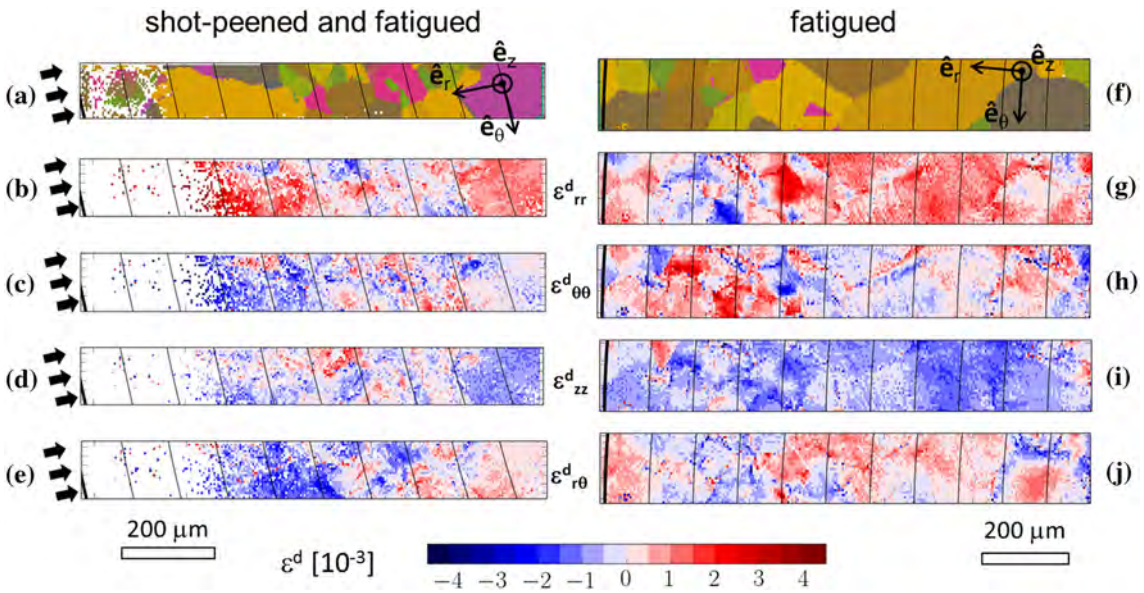

Figure 17 Grain orientation and deviatoric elastic strain components associated with **a**–**e** the shot-peened and fatigued sample S4, **f**–**j** the fatigued sample S5. The components are represented in the cylindrical coordinate system ($\hat{\mathbf{e}}_r$, $\hat{\mathbf{e}}_\theta$, $\hat{\mathbf{e}}_z$) related to the sample surface. They correspond to the average alloy ($\gamma + \gamma'$ phases). The sample edge is at left. The isoradius contour lines have a spacing of 100 µm. Arrows indicate the average direction of the shot-peening. A 5-µm step size was used during the µXRD measurements.

Table 3 Single-crystal elastic constants (in GPa) derived with the isotropic and anisotropic cubic elasticity from the isotropic Young modulus and Poisson's ratio related to the investigated samples

	C_{11}	C_{12}	C_{44}	E	ν	A
Isotropic	291	125	83	216	0.3	1
Cubic + Voigt	233	153	112	216	0.3	2.8
Cubic + Reuss	248	146	143	216	0.3	2.8

fixed quantities, the three elastic constants can be derived using the previous sets of equations:

$$\begin{cases} C_{11}^V = E \cdot \dfrac{A+4+(A-6)\nu}{(2+3A)(1+\nu)(1-2\nu)} & C_{11}^R = \dfrac{E}{5A} \cdot \dfrac{3A+2-(A+4)\nu}{(1-2\nu)(1+\nu)} \\ C_{12}^V = E \cdot \dfrac{A-1+(4+A)\nu}{(2+3A)(1+\nu)(1-2\nu)} & C_{12}^R = \dfrac{E}{5A} \cdot \dfrac{A-1+(3A+2)\nu}{(1-2\nu)(1+\nu)} \\ C_{44}^V = EA \cdot \dfrac{5}{2} \dfrac{1}{(2+3A)(1+\nu)} & C_{44}^R = \dfrac{E}{10} \cdot \dfrac{(2A+3)}{1+\nu} \end{cases} \tag{6}$$

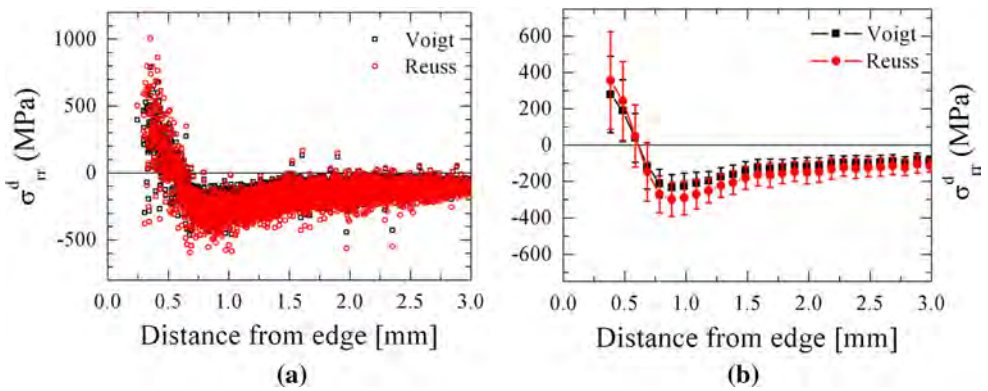

Figure 18 Profiles of the σ^d_{rr} deviatoric stress tensor component related to the shot-peened sample (S2) calculated with the set of elastic moduli corresponding to the Voigt (black squares) and Reuss (red circles) approximations (see text for detail). **a** shows all points of the stress map as a function of the distance from the shot-peened edge. **b** corresponds to the averaged profiles; the error bars are standard deviations.

The calculated values of $\{C_{ij}\}$ are listed in Table 3 for $E = 216$ GPa, $\nu = 0.3$ and $A = 2.8$. The effect of the approximation chosen to determine the elastic moduli is illustrated in Fig. 18 for the σ^d_{rr} deviatoric stress tensor component of the shot-peened sample S2. The figure represents the profile of σ^d_{rr} calculated from the strain map of Fig. 6b with the Voigt (black squares) and the Reuss (red circles) approximations. In Fig. 18a, all the data points of the map are represented as a function of the distance from the shot-peened edge of the sample. Figure 18b corresponds to the averaged profiles. Error bars represent the standard deviations. On the average over all data points, the relative difference between the Voigt and the Reuss approximations ranges from 20 to 23%. The mean value is 21% with a standard deviation of 0.3%.

References

[1] McClung R (2007) A literature survey on the stability and significance of residual stresses during fatigue. Fatigue Fract Eng Mater Struct 30(3):173–205

[2] Antolovich D (2015) Microstructural aspects of fatigue in Ni-base superalloys. Philos Trans R Soc A 373(2038):1–36

[3] Chaudonneret M (1993) A simple and efficient multiaxial fatigue damage model for engineering applications of macro-crack initiation. J Eng Mater Technol 115 115(4):373–379

[4] Boittin G, Locq D, Rafray A, Caron P, Kanouté P, Gallerneau F, Cailletaud G (2012) Influence of γ' precipitate size and distribution on LCF behavior of a PM disk superalloy. In: Superalloys 2012. Wiley, pp 167–176

[5] Korsunsky A (2005) The modelling of residual stresses due to surface peening using eigenstrain distributions. J Strain Anal Eng 40(8):817–824

[6] Cao W, Khadhraoui M, Brenier B, Guédou JY, Castex L (1994) Thermomechanical relaxation of residual stress in shot peened nickel base superalloy. Mater Sci Technol 10(11):947–954

[7] Khadhraoui M, Cao W, Castex L, Guédou J (1997) Experimental investigations and modelling of relaxation behaviour of shot peening residual stresses at high temperature for nickel base superalloys. Mater Sci Technol 13(4):360–367

[8] Evans A, Kim SB, Shackleton J, Bruno G, Preuss M, Withers P (2005) Relaxation of residual stress in shot peened Udimet 720Li under high temperature isothermal fatigue. Int J Fatigue 27(10–12):1530–1534 fatigue Damage of Structural Materials V5th International Conference on Fatigue Damage of Structural Materials

[9] John R, Buchanan D, Caton M, Jha S (2010) Stability of shot peen residual stresses in IN100 subjected to creep and fatigue loading. Procedia Eng 2(1):1887–1893

[10] Stone H, Reed R, Holden T (1999a) Determination of the plane specific elastic constants of Waspaloy using neutron diffraction. Scr Mater 40(3):1797–1808

[11] Stone H, Holden T, Reed R (1999b) On the generation of microstrains during the plastic deformation of Waspaloy. Acta Mater 47(17):4435–4448

[12] Connor L, Stone H, Collins D, Preuss M, Hardy M, Rae C (2014) The effect of cooling rate from solution on the lattice misfit during isothermal aging of a Ni-base superalloy. Metall Mater Trans A 45(5):2436–2444

[13] Preuss M, da Fonseca JQ, Grant B, Knoche E, Moat R, Daymond M (2008) The effect of γ' particle size on the deformation mechanism in an advanced polycrystalline nickel-base superalloy. Proceedings of superalloys 2008

[14] Buchanan D, John R (2008) Relaxation of shot-peened residual stresses under creep loading. Scr Mater 59(3):286–289

[15] Child D, West G, Thomson R (2011) Assessment of surface hardening effects from shot peening on a Ni-based alloy using electron backscatter diffraction techniques. Acta Mater 59(12):4825–4834

[16] Foss B, Gray S, Hardy M, Stekovic S, McPhail D, Shollock B (2013) Analysis of shot-peening and residual stress relaxation in the nickel-based superalloy RR1000. Acta Mater 61(7):2548–2559

[17] Messé O, Stekovic S, Hardy M, Rae C (2014) Characterization of plastic deformation induced by shot-peening in a Ni-base superalloy. JOM 66(12):2502–2515

[18] Viereck D, Lhe D, Vhringer O, Macherauch E (1991) Relaxation of residual stresses in nickel-base superalloy due to dislocation creep. In: International conference of strength of metals and alloys 9, Freund Publishing, pp 14–19

[19] Musinski W, McDowell D (2015) On the eigenstrain application of shot-peened residual stresses within a crystal plasticity framework: application to Ni-base superalloy specimens. Int J Mech Sci 100:195–208

[20] Barabash R, Ice G (2014) Strain and dislocation gradients from diffraction: spatially-resolved local structure and defects. Imperial College Press, London

[21] Kang K, Yao N, He M, Evans A (2003) A method for in situ measurement of the residual stress in thin films by using the focused ion beam. Thin Solid Films 443(1):71–77

[22] Korsunsky AM, Sebastiani M, Bemporad E (2009) Focused ion beam ring drilling for residual stress evaluation. Mater Lett 63(22):1961–1963

[23] Salvati E, Lunt A, Ying S, Sui T, Zhang H, Heason C, Baxter G, Korsunsky A (2017) Eigenstrain reconstruction of

residual strains in an additively manufactured and shot peened nickel superalloy compressor blade. Comput Methods Appl Mech Eng 320(Supplement C):335–351

[24] Benedetti M, Fontanari V, Winiarski B, Allahkarami M, Hanan J (2016) Residual stresses reconstruction in shot peened specimens containing sharp and blunt notches by experimental measurements and finite element analysis. Int J Fatigue 87(Supplement C):102–111

[25] Müller EMP (1961) Das $\sin^2\psi$-verfahren der röntgenographischen spannungsmessung. Z Angew Phys 13(7):305–312

[26] Ortner B (1983) Rontgenographische spannungsmessung an einkristallinen proben. In: Eingenspannungen, Deutsche Gesellschaft fur Metallkunde, Oberursel, pp 49–68

[27] Ortner B (1985) The choice of lattice planes in X-ray strain measurements of single crystals. Adv X-Ray Anal 29:113–118

[28] Morançais A, Fèvre M, François M, Guel N, Kruch S, Kanouté P, Longuet A (2015) Residual stress determination in a shot-peened nickel-based single-crystal superalloy using X-ray diffraction. J Appl Cryst 48(6):1761–1776

[29] Wlodek S, Kelly M, Alden D (1992) The structure of N18. In: SD Antolovich RM RW Stusrud (ed) Superalloys 1992, Wiley, pp 467–471

[30] Ulrich O, Biquard X, Bleuet P, Geaymond O, Gergaud P, Micha JS, Robach O, Rieutord F (2011) A new white beam X-ray microdiffraction setup on the BM32 beamline at the European Synchrotron Radiation Facility. Rev Sci Instr 82(3):033,908

[31] Robach O, Micha JS, Ulrich O, Gergaud P (2011) Full local elastic strain tensor from Laue microdiffraction: simultaneous Laue pattern and spot energy measurement. J Appl Cryst 44(4):688–696

[32] Micha JS, Robach O (2010). http://sourceforge.net/projects/lauetools/

[33] Larson B, Yang W, Ice G, Budai J, Tischler J (2002) Three-dimensional X-ray structural microscopy with submicrometre resolution. Nature 415(6874):887–890

[34] Yang W, Larson B, Tischler J, Ice G, Budai J, Liu W (2004) Differential-aperture X-ray structural microscopy: a submicron-resolution three-dimensional probe of local microstructure and strain. Micron 35(6):431–439

[35] Chung J, Ice G (1999) Automated indexing for texture and strain measurement with broad-bandpass X-ray microbeams. J Appl Phys 86(9):5249–5255

[36] Hofmann F, Eve S, Belnoue J, Micha JS, Korsunsky A (2011) Analysis of strain error sources in micro-beam Laue diffraction. Nucl Instrum Methods A 660(1):130–137

[37] Ice G, Chung J, Lowe W, Williams E, Edelman J (2000) Small-displacement monochromator for microdiffraction experiments. Rev Sci Instrum 71(5):2001–2006

[38] Send S, von Kozierowski M, Panzner T, Gorfman S, Nurdan K, Walenta AH, Pietsch U, Leitenberger W, Hartmann R, Strüder L (2009) Energy-dispersive Laue diffraction by means of a frame-store pnCCD. J Appl Cryst 42(6):1139–1146

[39] Robach O, Micha JS, Ulrich O, Geaymond O, Sicardy O, Härtwig J, Rieutord F (2013) A tunable multicolour 'rainbow' filter for improved stress and dislocation density field mapping in polycrystals using X-ray Laue microdiffraction. Acta Cryst A 69(2):164–170

[40] Lautridou JC, Guédou JY (1994) Heat treatment upgrading on PM superalloy N18 for high temperature applications. In: Coutsouradis D, et al (eds) Materials for advanced power engineering, Part II. Kluwer Academic Publishers, Dordrecht, pp 951–960

[41] Honnorat Y (1991) N18, damage tolerant nickel-based superalloy for military aircraft turbine discs. Mater Tech 79(5–6):19–30

[42] Chao J, Mark A, Fuller MS, McIntyre NS, Holt R, Klassen R, Liu W (2009) Study of residual elastic- and plastic-deformation in uniaxial tensile strained nickel-based alloy 600 samples by polychromatic X-ray microdiffraction (PXM) and neutron diffraction methods. Mater Sci Eng A 524(1–2):20–27

[43] Wright S, Nowell M, Basinger J (2012) Angular precision of automated electron backscatter diffraction measurements. In: Textures of materials—ICOTOM 16, Trans Tech Publications, Materials Science Forum, vol 702, pp 548–553

[44] Brough I, Bate PS, Humphreys FJ (2006) Optimising the angular resolution of EBSD. Mater Sci Technol 22(11):1279–1286

[45] Altinkurt G, Fèvre M, Robach O, Micha JS, Geandier G, Dehmas M (2017) Full elastic strain tensor determination at the phase scale in a powder metallurgy nickel-based superalloy using X-ray Laue microdiffraction. J Appl Cryst 50(6):1754–1765

[46] Salvati E, Korsunsky AM (2017) An analysis of macro- and micro-scale residual stresses of Type I, II and III using FIB-DIC micro-ring-core milling and crystal plasticity FE modelling. Int J Plast 98:123–138

[47] Voigt W (1928) Lehrbuch der Kristallphysik. Teubner

[48] Reuss A (1929) Berechnung der Fliessgrenze von Mischkristallen auf Grund Plastizitätsbedingung für Einkristalle. ZAMM-Z Angew Math Mech 9(1):49–58